# Epithelial development of the urinary collecting system in the human embryo

（ヒト胚における尿収集系の上皮形成）

Saizonou Omoloto Marie-Ange Joelle

PLOS ONE

RESEARCH ARTICLE

# Epithelial development of the urinary collecting system in the human embryo

**Marie Ange Saizonou[1], Haruka Kitazawa[1], Toru Kanahashi[1], Shigehito Yamada[1,2], Tetsuya Takakuwa[1]***

**1** Human Health Science, Kyoto University Graduate School of Medicine, Kyoto, Japan, **2** Congenital Anomaly Research Center, Kyoto University Graduate School of Medicine, Kyoto, Japan

* tez@hs.med.kyoto-u.ac.jp



OPEN ACCESS

**Citation:** Saizonou MA, Kitazawa H, Kanahashi T, Yamada S, Takakuwa T (2024) Epithelial development of the urinary collecting system in the human embryo. PLoS ONE 19(4): e0301778. https://doi.org/10.1371/journal.pone.0301778

**Editor:** Antoine Naem, University of Bremen: Universitat Bremen, GERMANY

**Received:** September 26, 2023

**Accepted:** March 21, 2024

**Published:** April 10, 2024

**Peer Review History:** PLOS recognizes the benefits of transparency in the peer review process; therefore, we enable the publication of all of the content of peer review and author responses alongside final, published articles. The editorial history of this article is available here: https://doi.org/10.1371/journal.pone.0301778



**Data Availability Statement:** Yes - all data are fully available without restriction All relevant data are within the manuscript and its Supporting information files.

## Abstract

The urinary collecting system (UCS) consists of organized ducts that collect urine from the nephrons and transport it to the ureter and bladder. Understanding the histogenesis of the UCS is critical. Thirty human embryos between the Carnegie stages (CS) 18 and 23 were selected from the Congenital Anomaly Research Center, Kyoto, Japan. Epithelia of the UCS, ureter, and bladder of each sample were randomly selected. Histological findings of the epithelia were analyzed according to the following criteria: type of epithelium, presence or absence of glycogen, percentage of migrated nuclei, percentage of cells in mitosis, and the surrounding mesenchyme. A thickened epithelium lining a narrow luminal cavity was observed in the pre-expanded pelvic specimens at CS18-CS23. At CS23, after pelvic expansion, the UCS showed a thin epithelium with a large luminal cavity mainly located on the early branches, whereas the epithelium covering the subsequent branches had medium thickness. Histological characteristics differed depending on the UCS part and sample stage. The degree of differentiation was evaluated, revealing that in CS18-CS23 pre-expanded pelvis specimens, the undifferentiated epithelium was found in the zeroth to third/fifth generation, whereas at CS23, after pelvic expansion, a differentiated epithelium covered the UCS zeroth to seventh generation. In a comparison of the urothelial epithelium between the UCS, ureter, and bladder, we found that urinary tract differentiation may be initiated in the bladder, followed by the ureter, UCS zeroth to seventh generations, and finally, UCS eighth to end generations. An understanding of the histogenesis of embryonic stage UCS can aid in the clinical management of congenital urinary tract defects and other diseases.

## Introduction

The uroepithelium or urothelium is an epithelial tissue that lines the distal portion of the urinary tract, including the renal pelvis, ureters, bladder, and upper urethra and is composed of apical, intermediate, and basal cell layers [1]. Functionally, it forms a distensible barrier that accommodates significant changes in urine volume while preventing unregulated exchange of substances between the urine and blood supply. In addition to its role as a barrier, the uroepithelium can modulate the movement of ions, solutes, and water across the epithelial tissue [2]. The uroepithelium is, thus, a dynamic tissue that responds to changes in its local environment and can relay this information to other tissues that comprise organs [1].

**Funding:** SPS KAKENHI (grant number JP 21K07772, JP 23K14976). The funders had no role in study design, data collection and analysis, decision to publish, or preparation of the manuscript.

**Competing interests:** The authors have declared that no competing interests exist.

The bladder epithelium is derived from the endoderm of the vesical part of the urogenital sinus. The ureter originates from the ureteric bud, a protrusion of the mesonephric duct, during the development of the genitourinary system. Several studies have described urothelial differentiation in the bladder and ureter. Previous studies have reported that the urothelium is pseudo-stratified. However, later studies showed that it is stratified and that cytoplasmic processes are observed, although rarely, in the intermediate cell layers but not in the basal cell layers [3]. Wesson [4] demonstrated that a single layer of low-cuboidal to high-columnar epithelium with prominent vesicular features lines the entire vesicoureteric anlage. Felix [5] stated that this single layer over the openings of the ureters develops into two or three layers by the end of the 6th week and four to five cells thick by the 9th week.

The urinary collecting system (UCS) is a significant component of the metanephros, and its developmental process is initiated from a simple epithelial tube [6]. The UCS arises from the iterative branching of this epithelial tube, resulting in a series of elaborate ducts that collect urine from all the nephrons and transfer it to the bladder via the urothelial duct. Oliver [7] and Al-Awqati et al. [8] described the UCS as a highly organized and regulated structure of ducts formed by bifid branching during the embryonic and fetal periods, where bifurcation occurs approximately 15 times. In stage CS23, the proximal UCS is remodeled into the renal pelvis and calyx, from which the collecting ducts are distributed [9–11]. This phenomenon divides late embryos into two categories: pre-expanded and expanded pelvis groups [12]. Several factors, including the development of nascent nephrons, their connection to the UCS, and the initiation of urinary excretion, may contribute to proximal UCS expansion [12, 13]. However, the mechanisms underlying proximal UCS expansion remain unclear. Potter et al. demonstrated an epithelium composed of tall columnar cells with large oval nuclei, surrounded by connective tissue, in early embryos [14]. In late embryos, the expansion of the first generation of branches presented a thin epithelium. Our group has provided a brief overview of histogenesis, mainly focusing on UCS morphogenesis and branching development [12]. Pelvic expansion could affect UCS histology and vice versa. Precise differentiation of UCS epithelium according to the number of generations is lacking. Recent studies using experimental mouse models have provided a histological atlas of the developing mouse urogenital system describing organogenesis and morphogenesis. It is unclear whether these observations can be applied to the human UCS, as the early branches of the UCS in late mouse embryos appear to be different from those in humans [15].

Although the urinary tract (including the ureter and bladder) is uniformly lined by the urothelium, the process of histological differentiation during the embryonic period is primarily confined to the bladder [2, 3, 16] and urinary tract [6], with detailed descriptions lacking for the UCS [12]. Because urine secretion initiates during the late embryonic period [17], clarifying the features and timeline of the histological differentiation of the urothelium region by region is essential. Clinically, this could yield data to ascertain the locations of congenital urinary tract defects, potentially facilitating the initiation of a clinical retrospective study on probable causes. Herein, we aimed to demonstrate the differentiation of the UCS epithelium in the human metanephros during the human embryonic period and to evaluate its degree of differentiation compared to that of the ureter and bladder epithelia.

## Materials and methods

### Ethics approval

The ethics committees of Kyoto University Faculty and Graduate School of Medicine, Japan, approved the use of human embryonic and fetal specimens for this study (approval number: R0316).

## Human embryonic specimens

At the Congenital Anomaly Research Center, Kyoto University Graduate School of Medicine, Japan, are stored in nearly 45,000 human specimens of embryos and fetuses, constituting the Kyoto Collection [18]. Most specimens were obtained when the pregnancy was terminated during the first trimester under the Maternity Protection Law of Japan. Samples were collected from 1961 to 1971, according to the regulations pertaining to each period (Table 1). For example, written informed consent was not required from parents back then; instead, verbal informed consent was sufficient to deposit the specimens, which was documented in medical records. All samples were anonymized and de-identified. Data were accessed for research purposes from Apr 1, 2021, to Mar 1, 2023. Approximately 20% of the specimens were undamaged and well-preserved. Embryos were measured, examined, and staged according to the criteria described by O'Rahilly and Müller [19]. Whole embryonic samples were fixed with 10% formalin, embedded in paraffin, and serially sectioned to a thickness of 10 μm. These samples were stained with hematoxylin and eosin (HE), and the specimens were preserved.

In this study, serial tissue sections were used from embryo specimens between CS18 and CS23 belonging to the Kyoto Collection ranging from 12.0 to 28.7 mm crown-rump length (CRL) (n = 30; five samples per stage) (Table 1).

## Digitalization of histological sections and metanephros 3-D reconstruction

Histological sections of the metanephros were digitalized, and three-dimensional (3D) reconstructions were generated as described previously [12]. Briefly, serial transverse sections (thickness, 10 μm) of whole embryos were digitalized using an Olympus virtual slide system (VS120-S5-J, Olympus Corp., Tokyo, Japan) for histological observations and 3D reconstructions. Sequential two-dimensional (2D) images at 25× magnification were digitally cropped around the metanephros. The metanephros, including the UCS, was segmented into serial digital sections. 3D images and the centerline of the UCS were computationally reconstructed and analyzed using Amira v. 5.5.0 (Visage Imaging GmbH, Berlin, Germany).

## Selection of histological sections for analyses of UCS epithelium as per the generation number, urothelial duct, and bladder

Using the reconstructed UCS tree, sections that included branches suitable for histological observations were selected. These sections included the transverse section of the branches in the middle, where the generation numbers could be identified. The selected images were cropped at 40× magnification and used for histological observation and analysis (Fig 1). Four transverse sections per generation of each sample were selected for further observation (Fig 1A and 1B).

**Urothelial duct.** Representative sections of the urothelial duct located at the ureteric-pelvic junction (UPJ) and bladder (distal section) were selected (Fig 1B). The selected images were cropped at 40× magnification and used for histological observation and analysis. Two transverse sections for each sample were selected for further observation.

**Bladder.** For each specimen, whole sections of the bladder, including anatomical landmarks, were identified. Suitable sections were cropped, magnified 40× on the bladder neck and dome regions, and used for histological observation and analysis (Fig 1B). Two sections from two samples each per stage were selected for further observation.

**Table 1. Samples used in the present study.**

| CS | ID | Collecting date | CRL | Orientation | Serial sections | | Urinary collecting branches | |
|---|---|---|---|---|---|---|---|---|
| | | | | | Total number | Kidney Range | Maximum number of generation | Total branches |
| **18** | 24992 | 14.02.1970 | 12 | Cr | 39 | 30–33 | 4 | 11 |
| | 28129 | 10.04.1971 | 13 | Cr | 50 | 37–43 | 4 | 15 |
| | 10309 | 1.06.1966 | 13.7 | Sa | 31 | 11–24 | 5 | 17 |
| | 15391 | 19.07.1967 | 14.2 | Lo | 26 | 12–21 | 2 | 5 |
| | 3901 | 17.08.1965 | 14.7 | Lo | 43 | 22–27 | 6 | 25 |
| **19** | 7168 | 02.02.1966 | 13.3 | Lo | 96 | 16–21 | 7 | 35 |
| | 16696 | 25.11.1967 | 13.7 | Cr | 55 | 47–49 | 7 | 27 |
| | 8389 | 21.06.1966 | 16.3 | Cr | 83 | 25–35 | 6 | 39 |
| | 3002 | 05.06.1965 | 18.4 | Cr | 87 | 70–75 | 7 | 37 |
| | 923 | 29.08.1963 | 17.5 | Sa | 39 | 13–30 | 7 | 58 |
| **20** | 2006 | 05.04.1965 | 15.9 | Cr | 62 | 58–59 | 7 | 59 |
| | 7271 | 19.02.1966 | 16.9 | Cr | 91 | 75–79 | 7 | 69 |
| | 4330 | 04.07.1965 | 18.6 | Cr | 87 | 75–78 | 7 | 90 |
| | 1580 | 08.01.1965 | 18.8 | Lo | 111 | 46–55 | 8 | 75 |
| | 567 | 12.04.1962 | 20.8 | Sa | 200 | 22–44 | 8 | 101 |
| **21** | 12155 | 27.10.1966 | 17.9 | Cr | 80 | 41–52 | 9 | 141 |
| | 16393 | 07.04.1967 | 18.7 | Cr | 60 | 46–51 | 8 | 141 |
| | 41 | 09.06.1961 | 19 | Cr | 98 | 44–57 | 9 | 102 |
| | 2021 | 30.03.1965 | 21.4 | Sa | 120 | 43–94 | 9 | 120 |
| | 2314 | 31.03.1965 | 22.6 | Cr | 142 | 69–93 | 9 | 160 |
| **22** | 8825 | 16.05.1966 | 21.3 | Cr | 115 | 65–83 | 10 | 182 |
| | 5685 | 17.11.1965 | 21.7 | Cr | 185 | 123–142 | 9 | 147 |
| | 9305 | 12.05.1966 | 22 | Cr | 96 | 79–86 | 11 | 286 |
| | 10444 | 12.08.1966 | 22.5 | Cr | 142 | 93–115 | 9 | 250 |
| | 5214 | 24.09.1965 | 23.4 | Cr | 201 | 103–135 | 11 | 333 |
| **23** | 3104 | 27.07.1965 | 25.2 | Lo | 137 | 96–113 | 9 | 216 |
| | 9005 | 23.04.1966 | 26 | Sa | 197 | 60–135 | 11 | 416 |
| | 4381 | 27.08.1965 | 26.3 | Sa | 198 | 26–104 | 11 | 480 |
| | 9026 | 03.06.1966 | 25.7 | Sa | 209 | 51–132 | 12 | 501 |
| | 12481 | 31.08.1966 | 28.7 | Sa | 205 | 104–190 | 12 | 397 |

CS, Carnegie stage; collecting date, date when the samples were first collected; CRL, crown-rump length; Cr, cross-section; Sa, sagittal section; Lo, longitudinal section; kidney range, serial sections where kidney was observed.

https://doi.org/10.1371/journal.pone.0301778.t001

## Evaluation of the UCS epithelium, urinary duct, and bladder

**Histological findings.** Histological findings of the UCS and transition side of the ureter were evaluated based on the criteria of a previous study describing the choroid plexus, with minor modifications [20, 21]. Characteristics of the UCS were selected based on these criteria, adapted, and reorganized according to our histological findings and the specificity of the UCS. These include 1) the type of epithelium (pseudostratified epithelium E1, simple cuboidal epithelium E2), 2) perinuclear glycogen in the cytoplasm (presence or absence), 3) percentage of migrated nuclei, 4) percentage of nuclei in mitosis, and 5) mesenchymal tissues surrounding the epithelium (loose connective tissue [CT], metanephric blastema [MB]) (Table 2).

Histological evaluation of the differentiation is not known for the human urothelium and is limited to another type of epithelium except for that of the choroid plexus [20, 21]. The

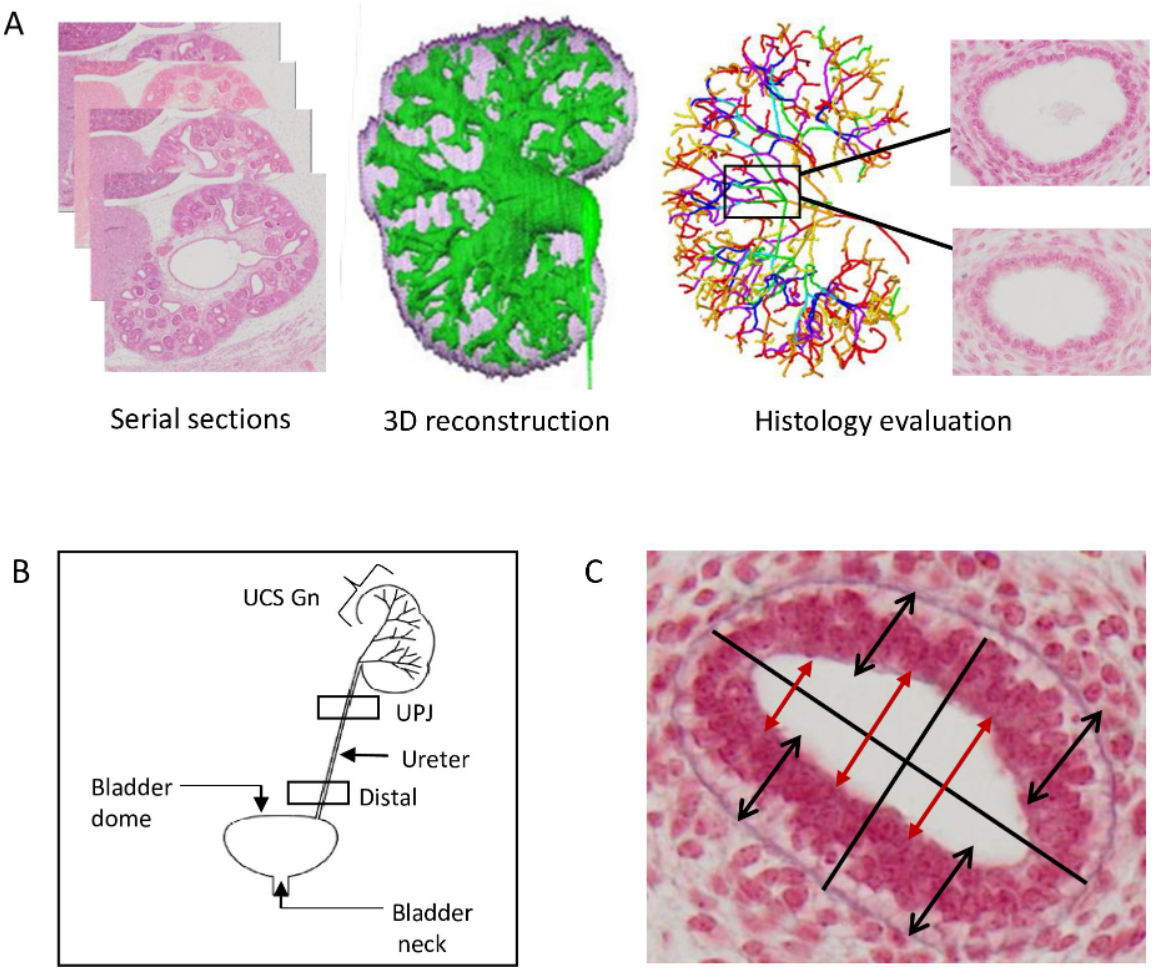


**Fig 1. Methods used in the present study.** (A) Selection of histological sections for the analysis of the urinary collecting system (UCS) epithelium according to the generation number. Three-dimensional reconstruction of metanephros and UCS centerline tree was used for histological evaluation. Representative generation branches were selected. Matched epithelium sections were cropped at 40× magnification. Illustrative data were obtained from a representative metanephros sample (CS23: ID 9026). (B) Illustration indicating the sections observed on the urinary tract. UPJ, ureteric pelvis junction; UCS Gn, urinary collecting system generation number. (C) Measurements of epithelium height and lumen diameter. The height of the epithelium and the size of the lumen are determined by averaging the lengths measured at four positions (indicated by black bidirectional arrows) and three positions (indicated by red bidirectional arrows) on the UCS, respectively.

https://doi.org/10.1371/journal.pone.0301778.g001

choroid plexus is a special organ that produces cerebrospinal fluid and is responsible for an important biological barrier system, forming an interface between the blood and the cerebrospinal fluid. Considering the urothelium's several functions described above, some physiological similarities in both structures appear evident. Therefore, it seemed interesting to use a similar differentiation criterion to describe epithelial tissue on the urinary tract whilst including its distinctive features.

The differentiation score in the UCS was calculated by the sum of the scores from each criterion.

The distribution of nuclei within the epithelium, observed in both apical-central and apical-central-basal regions—a characteristic akin to that of apically migrated nuclei—served to enrich the characterization of the ureteral epithelium.

**Table 2. Histological characteristics and differentiation scores of the UCS.**

| Structure | State | Score 0/0.5 | Score 1 |
|---|---|---|---|
| **Epithelium** | **Type** | Pseudostratified epithelium (E1)<br>Epithelium covered by a disposition of crowded oval nuclei located in various positions | Simple cuboidal epithelium (E2)<br>Epithelium lined by simple cuboidal cells |
| | **Glycogen** | Absence G (-)<br>Perinuclear substance inside the cytoplasm absent | Presence G (+)<br>Perinuclear substance inside the cytoplasm present |
| **Nuclei** | **Apical migrated nuclei** | High (>40%)<br>Intermediate ([15%–40%])<br>Percentage of apical migrated nuclei greater than 40% (Score 0)<br>Percentage of apical migrated nuclei ranged between [15%–40%] (Score 0.5) | Low (< 15%)<br>Percentage of apical migrated nuclei less than 15% |
| | **Percentage of nuclei in mitosis** | High (> 2%)<br>Percentage of nuclei in mitosis greater than 2% | Low (< 2%)<br>Percentage of nuclei in mitosis less than 2% |
| **Mesenchymal tissue surrounding the epithelium** | **Connective tissue/ Metanephric blastema** | Metanephric blastema (MB)<br>Mesenchyme surrounding UCS: metanephric blastema | A loose connective tissue (CT)<br>Loose connective tissue surrounding UCS |

https://doi.org/10.1371/journal.pone.0301778.t002

The bladder epithelium was observed at the neck and dome based on previous criteria [20, 21], according to the following histological findings: 1) type of epithelium (single layer epithelium [SL]), bi-layered epithelium [BL], multilayered epithelium [ML]), 2) perinuclear glycogen in the cytoplasm (present or absent), 3) presence of nuclei in mitosis, and 4) mesenchymal tissues surrounding the epithelium.

**Measurements.** The epithelial height and lumen diameter were measured in two selected sections per generation of branches in each sample. Two perpendicular lines, that is, the long and short axes, were determined. The epithelium height was measured parallel to the short axis at four positions. The epithelium height was calculated as the mean of the four lengths (Fig 1C). The lumen diameter was measured parallel to the short axis at three points and was calculated as the mean of the three lengths.

## Results

### 3D reconstruction of the UCS tree

3D reconstruction of the UCS tree revealed growth during the embryonic period (Fig 2), with an increase in the number of UCS generations and total branches. The maximum generation number (and ranges) of UCS end branching at each stage were as follows: CS18, 4.2 [2–6]; CS19, 6.6 [6–7]; CS20, 7.2 [6–8]; CS21, 8.8 [8–9]; CS22, 9.4 [9–10]; CS23P, 10.6 [10–11]; and CS23E, 11.0 [10–12]. The medians (and range) of the total number of UCS branches by the sixth to end generations (shown in orange in Fig 2) were as follows: CS18, 0.4 [0–2]; CS19, 7 [2–17]; CS20, 21.8 [10–47]; CS21, 63.4 [43–91]; CS22, 177.4 [87–268]; CS23P, 326.0 [140–420], and CS23E, 392.0 [334–450] (See also Table 1).

### Epithelium height according to growth

The epithelial height between CS18 and CS21 was approximately distributed between 20–25 μm, accompanied by an increase in generation number (Fig 3A). It markedly increased in the first to second generations at CS22, reached the local maximum at the second generation, and gradually decreased with an increase in the generation number. A similar trend was

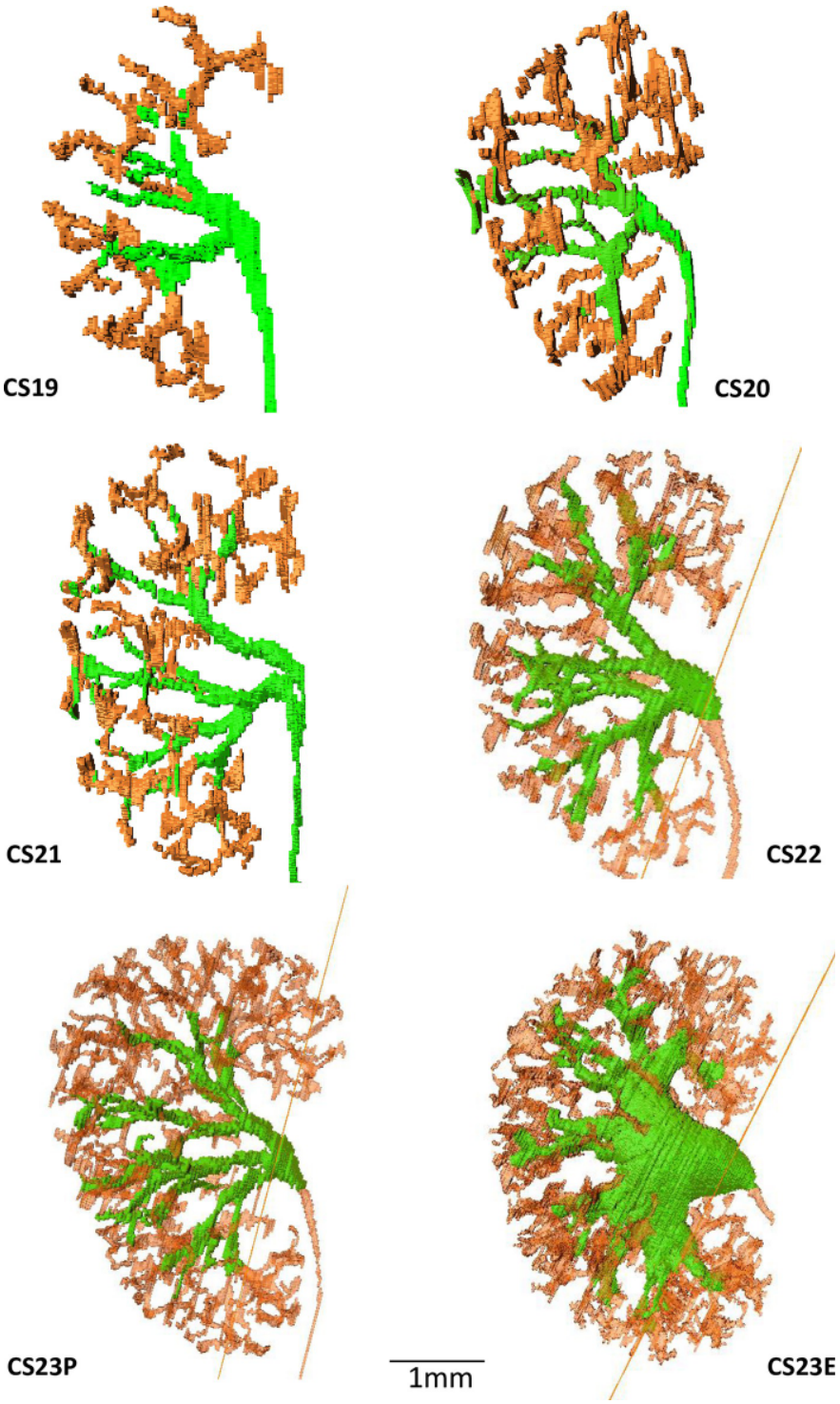


**Fig 2. Three-dimensional reconstruction of metanephros at stages CS18-CS23.** Green, zeroth to the fifth generation; orange, sixth to the end generation. The specimens at CS23 are divided into two categories: the pre-expanded pelvis group (CS23P) and the expanded pelvis group (CS23E), leading to an enlargement of the pelvis. Data was obtained from representative specimens at each Carnegie stage (CS19: ID923, CS20: ID567; CS21: ID2021; CS22: ID5685; CS23: ID9026).

https://doi.org/10.1371/journal.pone.0301778.g002

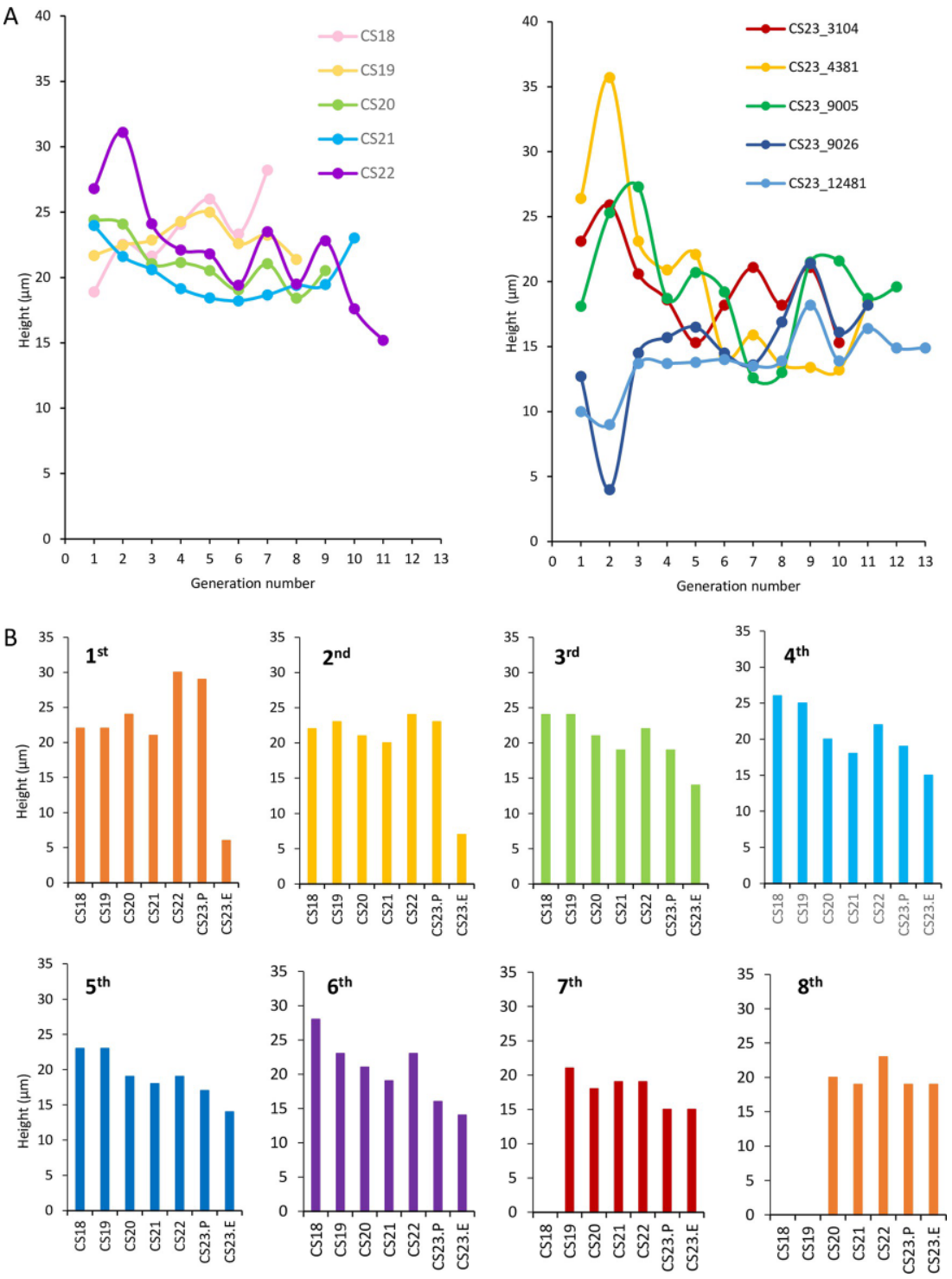


**Fig 3. Epithelium height in the UCS in relation to generation number.** (A) Change in the epithelium height according to the generation number. The mean thickness vs. generation number between CS18 and CS22 is indicated on the left, and the data value at each sample at CS23P and CS23E is indicated on the right. (B) Comparison of the epithelium heights between CS18 and CS23E by generation number. CS, Carnegie stage; CS23.P, Carnegie stage 23 pre-expanded pelvis; CS23.E, Carnegie stage 23 expanded. The measurement data was provided in S1 Data.

https://doi.org/10.1371/journal.pone.0301778.g003

observed at CS23P. The epithelial height markedly decreased from the first to the seventh generations at CS23E, mainly from the first to the fourth generations, with a local minimum observed in the second generation.

The epithelial heights of each generation were compared. In the first generation, the epithelial height showed a small local maximum at CS22 and CS23P. In the second and peripheral generations, epithelial height decreased as the stage increased, whereas the local maximum at CS22 became inconspicuous (Fig 3B).

## Lumen size according to growth

The average cavity size between CS18 and CS21 was almost similar (10–20 μm), slightly decreasing as the generation number increased. The lumen size increased from the first to fourth generations in the two samples of CS23P (Fig 4A). Lumen size increased with each generation of CS23E. The increase in lumen size was more prominent at CS23E than at CS18 -CS23P (Fig 4B).

## Comparison of epithelium height and lumen size by generation number

In the previous stages, between CS18 and CS23P, epithelial thickness and lumen size did not correlate, and lumen size was almost constant, regardless of epithelial thickness. At CS23E, the UCS showed a thin epithelium with a large luminal cavity, and its distribution differed from that in the previous stages (Fig 5). The trend was similar in all scatter plots for each generation number.

## Histological evaluation

**Epithelium type.** The UCS epithelium between CS18 and CS23P consisted of crowded oval nuclei located at various positions and a pseudostratified epithelium (E1) until their respective end branches. The epithelium on CS23E was lined with a superficial layer of cuboidal cells (E2), well-aligned around the lumen from the zeroth to the seventh generation. In contrast, the seventh-end generation exhibited characteristics similar to those of E1.

**Glycogen.** The perinuclear transparent substance glycogen, which appeared to repel the nuclei towards the apical side, was observed from the zeroth to second generations at CS18, from the zeroth to the fifth generations at CS19 and CS23P, and from the zeroth to the sixth generation at CS23E. Glycogen was not observed in the peripheral epithelium.

**Apical migrated nuclei and nucleus position.** At CS18-CS23P, nuclei were distributed mainly at the apical-central-basal position in the epithelium in the zeroth to end generations. The percentage of apical migrated nuclei in each epithelial layer was high through generations, ranging from 40% to 45%. At CS23E, nuclei were distributed mainly at the apical-central position in the epithelium from the zeroth to seventh generations and at the apical-central-basal position between the eighth to twelfth generations. The percentage of apical nuclei was lower in the zeroth to seventh generations (3%–15%), increasing slightly in the eighth to end generations (12%–28%), and remained lower than in embryos between CS18 and CS23P.

**Percentage of nuclei in mitosis.** In most regions of CS18 and CS20 and the peripheral regions of CS19 and CS23E, mitosis was observed in more than 2% of the epithelial cells. Mitosis was observed in less than 2% epithelia, mainly in the proximal part of the UCS, with several exceptions between CS21 and CS23E, namely, zeroth to fourth generations at CS21, zeroth to fifth generations except for first and second generation at CS22, and zeroth to sixth generations at CS23P and CS23E.

**Mesenchymal tissue surrounding the epithelium.** Loose connective tissue surrounded the UCS epithelium in the zeroth to second generations at CS18, fourth generation at CS19

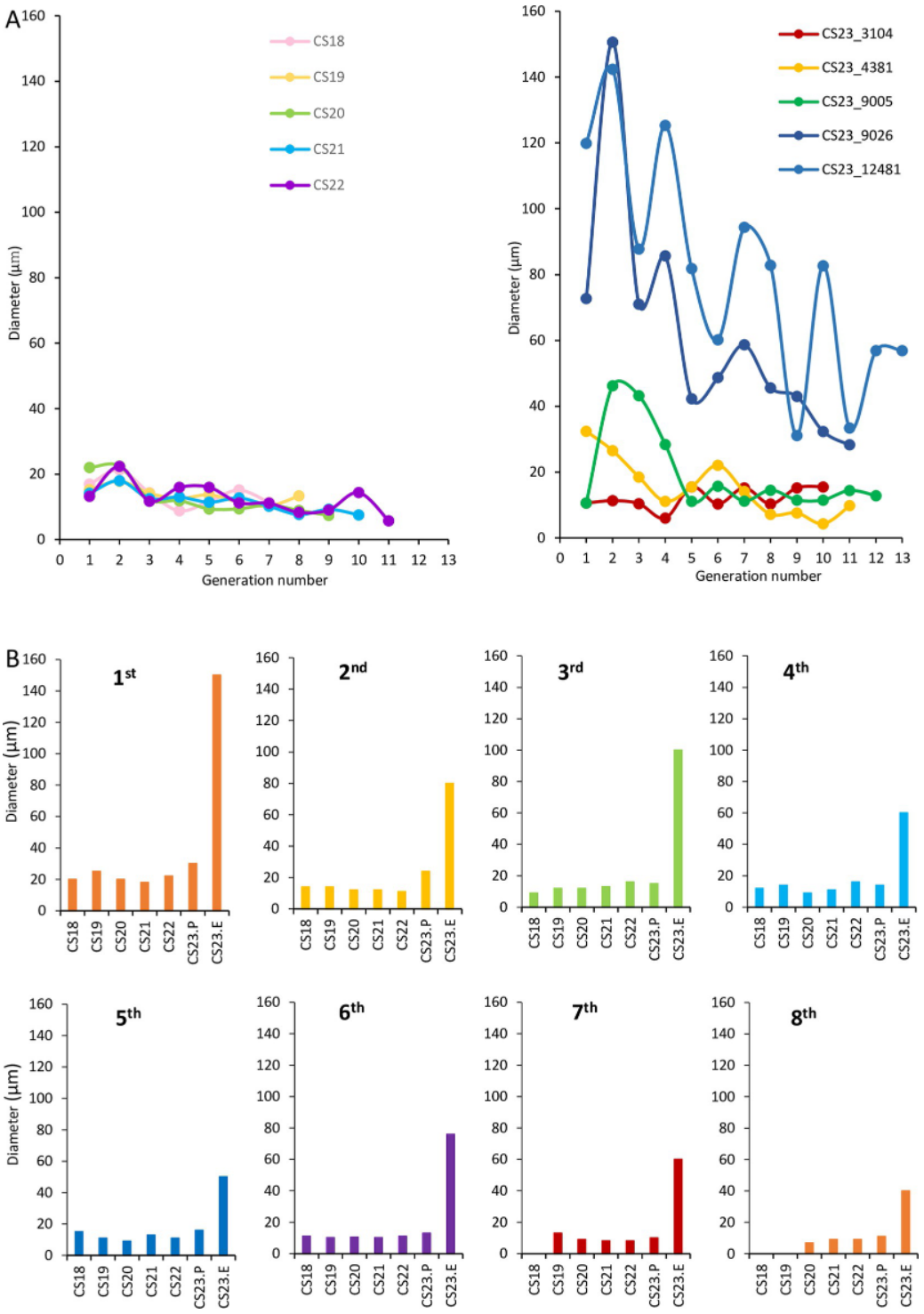


**Fig 4. Lumen size in the UCS according to generation number.** (A) Change in the lumen size according to the generation number. The mean lumen size vs. generation number between CS18 and CS22 is indicated on the left, and the data values for each sample at CS23P and CS23E are indicated on the right. (B) Comparison of the epithelium lumen sizes between CS18 and CS23E by each generation. CS, Carnegie stage; CS23P, Carnegie stage 23 pre-expanded pelvis; CS23E, Carnegie stage 23 expanded. The measurement data was provided in S2 Data.

https://doi.org/10.1371/journal.pone.0301778.g004

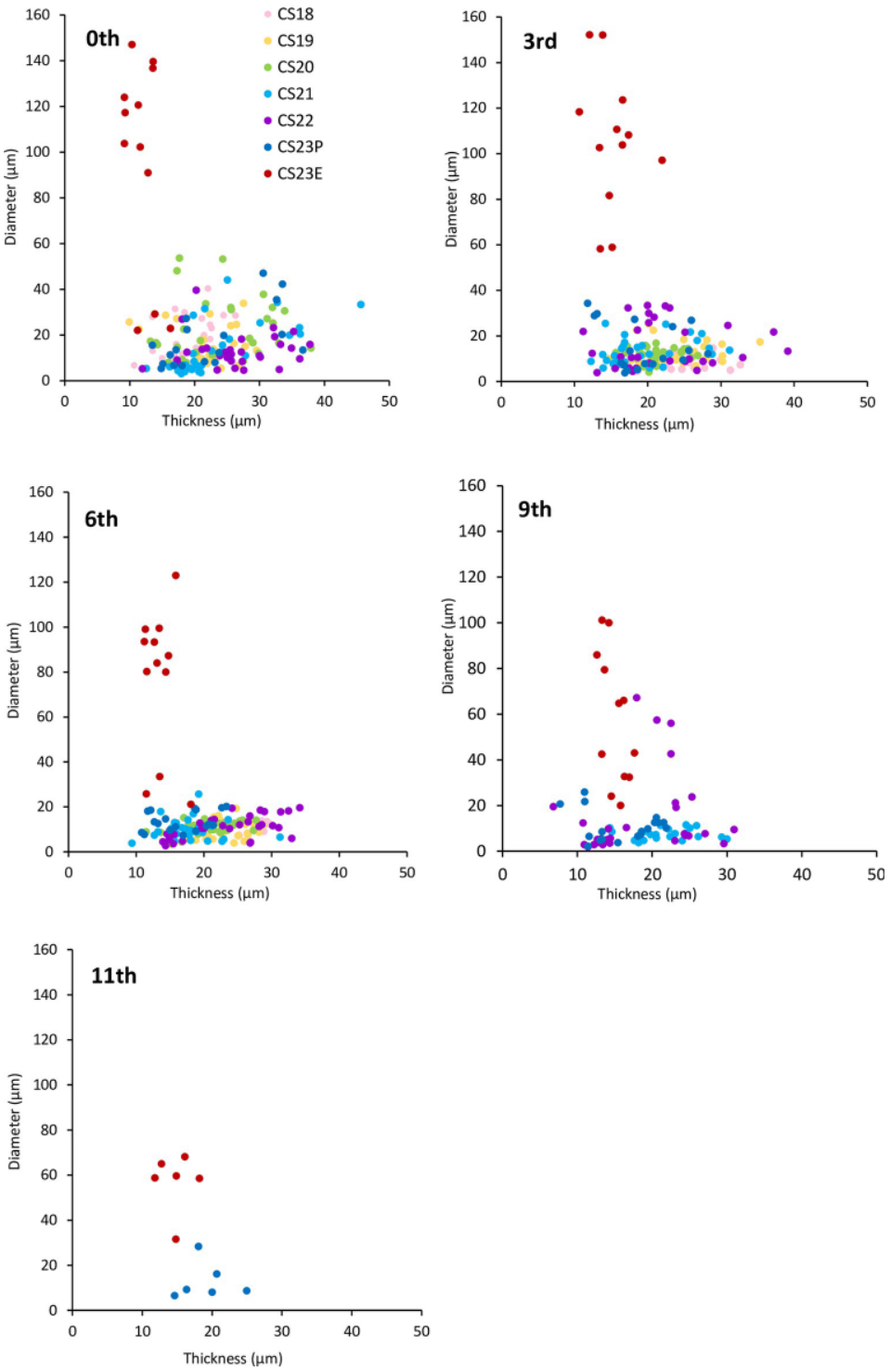


**Fig 5. Scatter plots showing the relationship between epithelium height and lumen size of the UCS during CS18-CS23E.** Scatter plots are provided for five representative generation numbers: 0th, 3rd, 6th, 9th, and 11th. The measurement data was provided in S3 Data.

https://doi.org/10.1371/journal.pone.0301778.g005

and CS20, zeroth to sixth generations at CS21, and zeroth to seventh generations at CS22, CS23P, and CS23E. The metanephric blastema surrounded the subsequent peripheral branches.

### Differentiation score

The differentiation score of the UCS epithelium in each generation was calculated as the sum of the differentiation degrees in the five criteria mentioned earlier (Table 2). The histological features and differentiation in the proximal UCS region differed from those in the peripheral regions, depending on the specimen's embryonic stage (Fig 6A). The differentiation score increased according to the increase in CS and was higher in the proximal region than in the peripheral region. The score was high in the zeroth to seventh generations for CS23E. Representative histological pictures corresponding to the highlighted rectangle in the panel in Fig 6B were presented in Fig 7.

### Ureter

Glycogen-rich epithelium (G(+)) and surrounding loose connective tissue (CT) were observed at all stages, at both the junctional and distal sides (Fig 8A). Nuclei were distributed mainly at the apical-central-basal position in the epithelium between CS18 and CS22 and at the apical-central position at CS23P and CS23E at both the junctional and distal sides. Pseudostratified epithelium (E1) was observed between CS18 and CS23P at both the junctional and distal sides. At CS23E, a single cuboidal epithelium (E2) was observed at the junction side (close to the pelvis). Single cuboidal and bilayered epithelium was observed on the distal side (close to the bladder). The representative histological pictures are presented in Fig 8B.

### Bladder

Glycogen-rich epithelial wall (G(+)) and surrounding loose CT were observed at all stages in both the dome and neck of the bladder (Fig 9A). The bladder epithelium appeared to be different from that observed in the UCS, with progressive differentiation. The epithelium at CS18-CS19 was lined by a glycogen-rich, superficial layer of cells at the dome of the bladder and by multilayer cells at the neck of the bladder. At the bladder dome, the number of layers increased with growth; a BL was observed from CS19 onwards, and a tri-layered epithelium was observed from CS21 onwards. At all stages, the neck of the bladder was covered with ML. The representative histological pictures are presented in Fig 9B.

## Discussion

The urothelium lines the urinary tract, from the metanephros to the urethra. Previous studies on urothelial histology mainly focused on the bladder [5, 16] and urethra [4]. Newman and Antonakopoulos [16] reported that the proximal bladder epithelial layers progressively increase from a monolayer to a bilayer and then to a trilayer epithelium. Wesson [4] reported that a single layer of low-cuboidal to high-columnar cells lines the ureteral structure. These classical studies shed light on the general histological differentiation of the urothelium.

Few studies have focused on urothelial differentiation in the UCS. Potter [14] focused mainly on kidney morphogenesis and the spatial distribution of UCS branches and nascent nephrons. Limited observations have been made of the UCS epithelium, namely the pseudostratified epithelium, which suggests the presence of a multilayered epithelium. Lindström et al. reported on the 3D morphogenesis of the kidney by comparing human and mouse kidneys [15]. In UCS histology, a pseudostratified ureteral epithelial branch tip was observed at stages

A

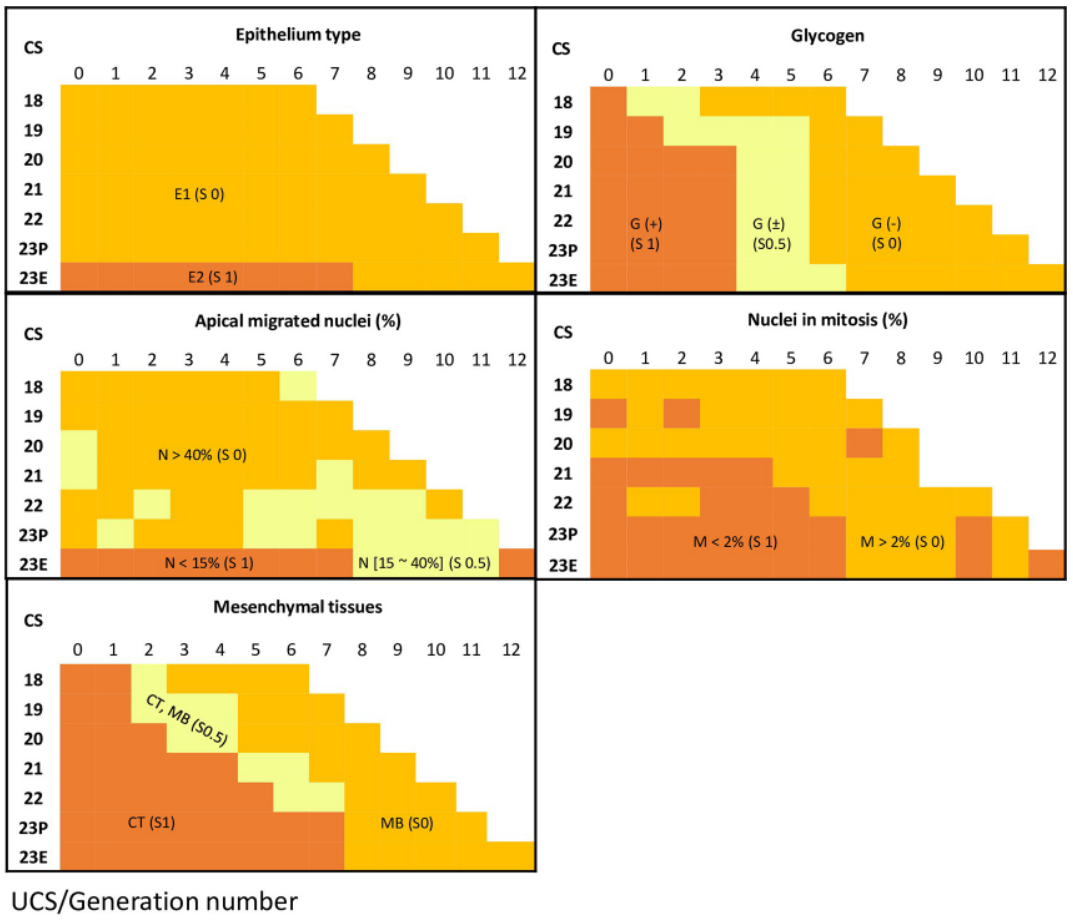


B

| CS | 0th | 1st | 2nd | 3rd | 4th | 5th | 6th | 7th | 8th | 9th | 10th | 11th | 12th |
|---|---|---|---|---|---|---|---|---|---|---|---|---|---|
| 18 | 2 | 1.5 | 2 | 0 | 0 | 0 | 0.5 | | | | | | |
| 19 | 3 | 2 | 2 | 1.5 | 1.5 | 0.5 | 0 | 0 | | | | | |
| 20 | 2.5 | 2 | 2 | 1.5 | 1 | 0.5 | 0 | 1 | 0 | | | | |
| 21 | 3.5 | 3 | 3 | 3 | 2.5 | 1 | 0.5 | 0.5 | 0 | 0 | | | |
| 22 | 3 | 2 | 2.5 | 3 | 2.5 | 3 | 1 | 1 | 0.5 | 0.5 | 0 | | |
| 23P | 3 | 3.5 | 3 | 3 | 2.5 | 3 | 2.5 | 0 | 0.5 | 0.5 | 1.5 | 0.5 | |
| 23E | 5 | 5 | 5 | 5 | 4.5 | 4.5 | 4.5 | 3 | 0.5 | 0.5 | 1.5 | 0.5 | 2 |

**Fig 6. Histological examination according to the Carnegie stage and generation number.** (A) Each panel indicates the type of epithelium, presence of glycogen, percentage of migrated nuclei, percentage of cells in mitosis, and mesenchyme surrounding the epithelium. Each criterion is explained in the Materials and Methods section. (B) The differentiation score was obtained from the six histological examinations. Histological images used in Fig 7 are highlighted by rectangles.

https://doi.org/10.1371/journal.pone.0301778.g006

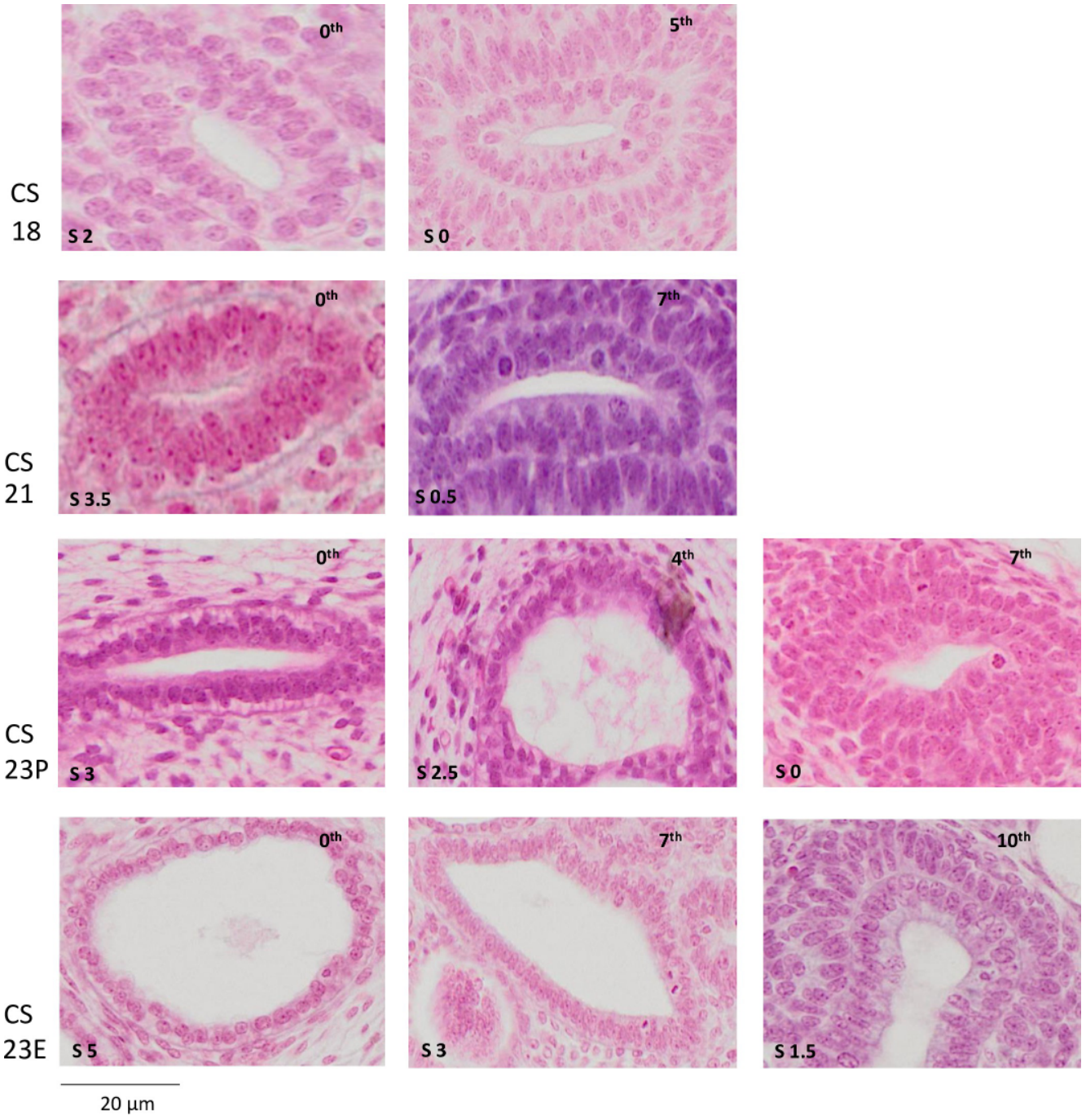


**Fig 7. Representative histological images depicting the UCS differentiation scores (S).** The generation number is mentioned in each image. Histological images presented here are highlighted by rectangles in Fig 6.

https://doi.org/10.1371/journal.pone.0301778.g007

CS16-CS19. The present study was unique in that the histogenesis of the urothelium was highlighted in the whole urinary tract, consisting of the UCS, ureter, and bladder, stage-by-stage, during the embryonic period. Moreover, this enabled comparisons of differentiation within the bladder, urinary tract, and UCS, as well as among these three, on the differentiation

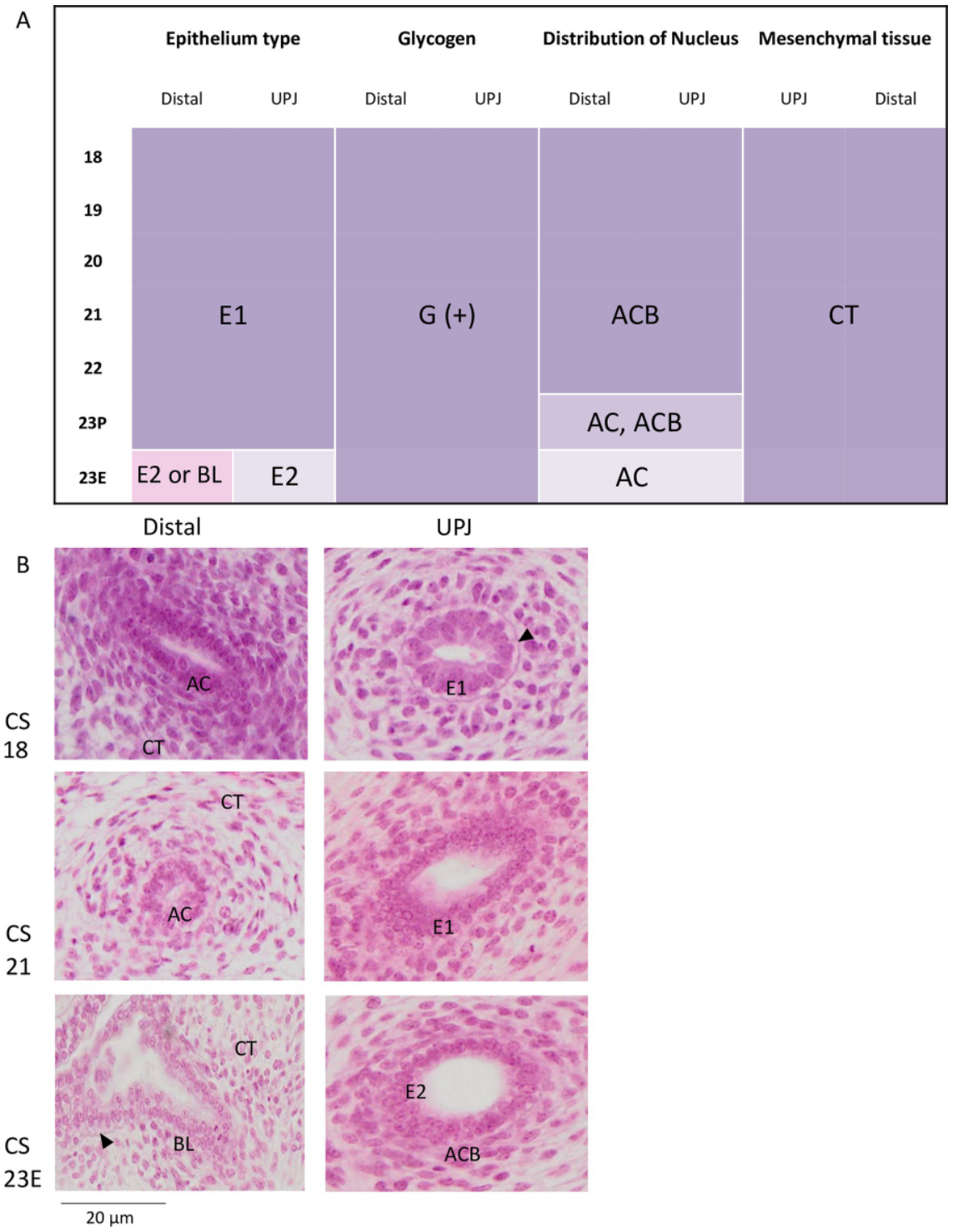


**Fig 8. Histological findings in the ureter.** (A) Panels indicate the epithelium type, presence of glycogen, nuclei position, and surrounding mesenchyme at the junction and the peripheral side. (B) Representative histological images of the ureter. E1, pseudostratified epithelium; E2, simple cuboidal epithelium; BL, bi-layered epithelium; G, glycogen; AC, apical-central; ACB, apical-central-basal; CT, connective tissue. Purple (in A) indicates the repartition of each feature by the Carnegie stage. Arrowheads indicate glycogen. Numbers represent Carnegie stage (CS); images shown on higher magnification (40×) ureter epithelium; scale bar = 20 μm. UPJ; ureteric pelvic junction, Distal; the distal side of the ureter.

https://doi.org/10.1371/journal.pone.0301778.g008

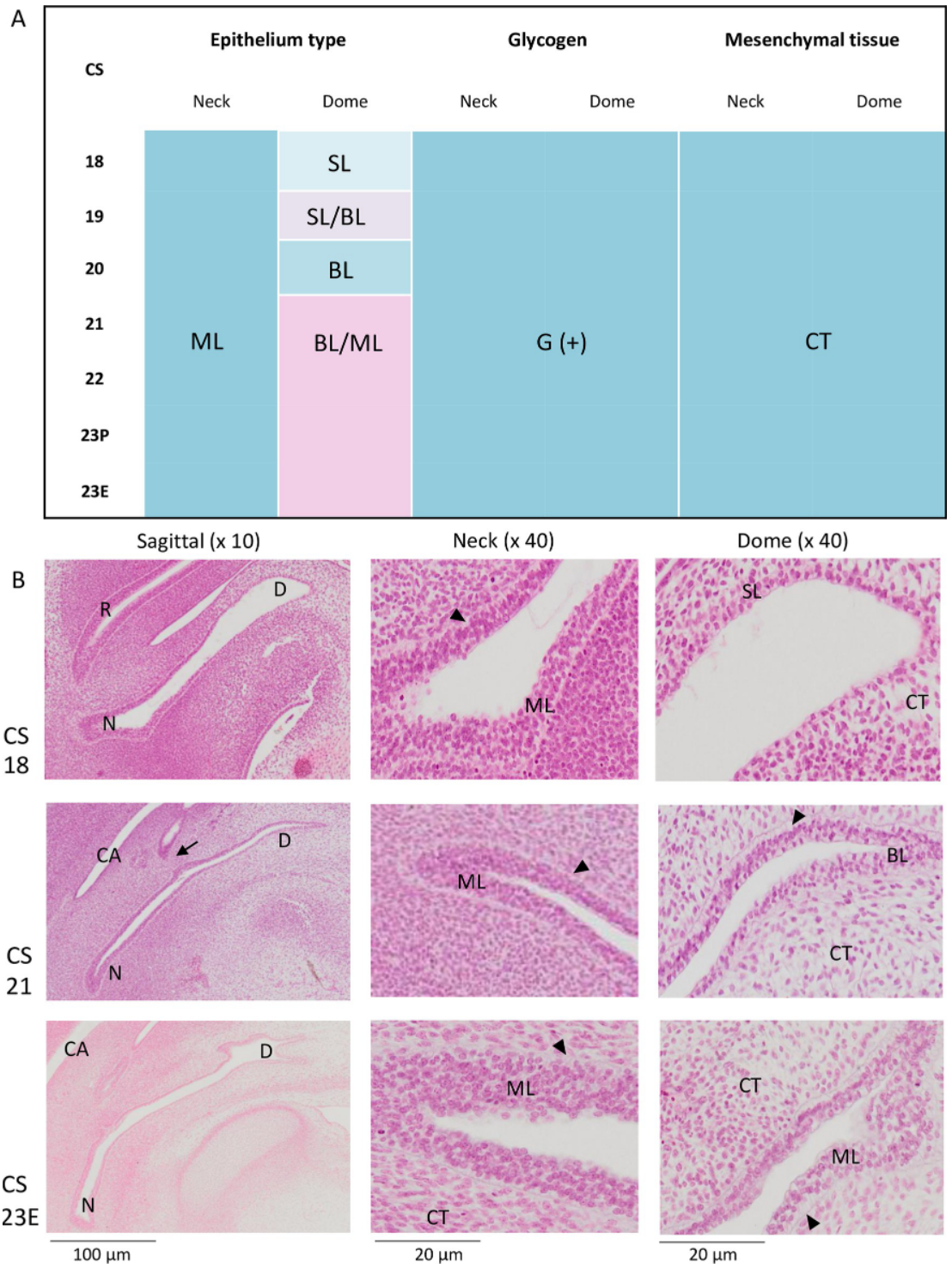


**Fig 9. Histological findings on the bladder.** (A) The panel indicates the epithelium type, presence of glycogen, and surrounding mesenchyme at the neck and dome of the bladder. SL, single layer; BL, bi-layers; ML, multilayers; G, glycogen; CT, connective tissue. (B) Representative histological images at CS18, CS21, and CS23E from the whole bladder (left), magnified neck (middle), and dome region (right). Arrows indicate the opening of the ureter. From left to right, respectively: lower magnification (10×) of sagittal section of whole bladder, scale bar = 100 μm; higher magnification (40×) showing neck and dome of bladder epithelium, scale bar = 20 μm. D, dome; N, neck; R, rectum; CA, abdominal cavity.

https://doi.org/10.1371/journal.pone.0301778.g009

timeline. We have described the UCS differentiation in detail, and specifically in the epithelium by each generation number.

In the UCS, the differentiation score decreased from the proximal to peripheral parts (with increasing generation number), regardless of the Carnegie stage. This trend was more pronounced for CS23E. In the distal ureter, the epithelium resembled that of the bladder. Contrastingly, the epithelium mirrored that of the UCS in the transitional region at CS23E, suggesting that the epithelial differentiation was more pronounced in the distal region than in the transitional area at CS23E. By CS18, the bladder epithelium in the neck region had become multilayered, evolving from a monolayer into a multilayered structure at the dome between CS18 and CS23.

The bladder neck epithelium at CS18-CS19 was comparable to the UCS epithelium in the zeroth to seventh generations at CS23E. Our findings suggest that the initial differentiation of urothelial cells may occur in a retrograde manner across the urinary tract, beginning with the bladder, followed by the ureter, and subsequently, the UCS.

A pseudostratified epithelium was observed at CS18-22, as described in previous studies [14, 15]. We observed and quantified the position of nuclei in the pseudostratified epithelium as an indicator of differentiation. The nuclei frequently migrated to the apical side of the UCS epithelium at stages CS18-CS23P, affecting approximately 45% of the nuclei. This migration observed in our study could correspond to the partial interkinetic nuclear migration (INM) noted in the ureter [22] and several digestive organs [23].

Makiko hypothesized that INM is a general strategy for epithelial progenitor expansion, although discrepant hypotheses have also been proposed [24].

The present study is the first to investigate the histology of the UCS after pelvic expansion (CS23E). The UCS at CS23E was completely different from that at previous stages, as noted in the 3D reconstruction and histological findings. In the previous stages, the epithelial thickness and lumen size were not correlated, and the latter was primarily constant regardless of the former. At CS23E, the UCS showed a thin epithelium with a large luminal cavity.

Although the expansion in the proximal region was striking, size expansion was simultaneously observed up to the terminal branch at CS23E. In contrast, differentiation timing at the UCS periphery occurred last in comparison to the rest of the urinary tract. This expansion may indicate the initiation of the physiological function of the urinary tract and the excretion of urine. Potter hypothesized that urinary secretions contribute to the expansion of the pelvis and calyces [8]. Several studies have shown that glomerular filtrate may increase the UCS pressure, forcing it to expand rapidly. We detected nephrons from CS19 and found that the total number of nephrons, and those connected to the UCS, increased until CS23 [12]. The human metanephros contributes to amniotic fluid volume at CS23 or earlier [17]. Lindström et al. [15] indicated that glomerular filtration may occur at CS23.

A previous study on the differentiation of the choroid plexus demonstrated that the histological findings, including the type of epithelium, presence of glycogen, position of nuclei, percentage of cells in mitosis, and surrounding mesenchyme, changed during the embryonic period between CS18 and CS23 [24]. These changes correspond to Netsky's Stages I and II, the first two of the four stages of differentiation [20, 21]. In the present study, most of these criteria were used to estimate urothelial differentiation during the same embryonic period. This means that urothelial and columnar (secretory) epithelia show similar findings during initial differentiation with a similar timeline in the human embryonic period. The airway epithelium shows findings similar to those of UCS. In 7-week embryos, the airways are lined by a thick pseudostratified endodermal epithelium in a bed of abundant loose mesenchyme; at 8 weeks, the airways enlarge and are covered by a simple columnar ciliated epithelium with prominent vacuoles [25]. The squamous epithelium of the skin shows an undifferentiated monolayer of

epithelium with glycogen and various mitoses in seven-week embryos [26]. The present study suggests that the histological findings during the initial UCS differentiation are similar to those of other epithelia, including secretory and squamous epithelia with similar timelines.

Three issues need consideration in this study. First is the effect of long-term storage on the subjects. Second, while tissue sections facilitate detailed observation, our quantitative histological analysis, employing formalin- and paraffin-embedded materials, may have been susceptible to errors. These errors could arise from degeneration during specimen handling, shrinkage due to fixation, and shearing during sectioning. Third, four suitable transverse sections were selected for each generation per sample. Accurate transverse sections were sometimes difficult to obtain in younger generations (proximal part) because the number of branches was limited.

## Conclusion

This study investigated the development of the UCS, ureter, and bladder epithelia during embryonic development. Our research detailed several features of the UCS epithelium according to generation number and embryonic stage. The differentiation scores of the epithelia reveal that the initial urothelial differentiation proceeds in a retrograde fashion in each region of the urinary tract. The present study provided histological data on the human urinary tract using embryos. Further study focusing on the histological development of the urinary tract in the fetus would be necessary to complete the chronology of UCS, ureter, and bladder histological development from conception to birth.

## Supporting information

**S1 Data.**
(XLSX)

**S2 Data.**
(XLSX)

**S3 Data.**
(XLSX)

## Acknowledgments

The authors thank Ms. Chigako Uwabe at the Congenital Anomaly Research Center for technical assistance in handling human embryos.

## Author Contributions

**Conceptualization:** Tetsuya Takakuwa.

**Data curation:** Marie Ange Saizonou, Haruka Kitazawa, Shigehito Yamada.

**Formal analysis:** Marie Ange Saizonou, Haruka Kitazawa.

**Methodology:** Toru Kanahashi.

**Supervision:** Tetsuya Takakuwa.

**Writing – original draft:** Marie Ange Saizonou.

**Writing – review & editing:** Tetsuya Takakuwa.

## References

1. Khandelwal P, Abraham SN, Apodaca G. Cell biology and physiology of the uroepithelium. Am J Physiol Renal Physiol. Dec. 2009; 297: F1477–F1501. [Epub 2009 Jul 8]. https://doi.org/10.1152/ajprenal.00327.2009 PMID: 19587142.
2. Lewis SA. Everything you wanted to know about the bladder epithelium but were afraid to ask. Am J Physiol Renal Physiol. 2000; 278: F867–F874. https://doi.org/10.1152/ajprenal.2000.278.6.F867 PMID: 10836974
3. Jost SP, Gosling JA, Dixon JS. The morphology of normal human bladder urothelium. J Anat. 1989; 167: 103–115. PMID: 2630525
4. Wesson MB. Anatomical, embryological and physiological studies of the trigone and neck of the bladder. J Urol. 1920; 4: 279–315. https://doi.org/10.1016/S0022-5347(17)74143-2
5. Felix W, Ch. XIX. The development of the urinogenital organs. In: Keibel F, Mall FP, editors. Manual ofHuman embryology, Vol. 2. Philadelphia: Lippincott & Crowell; 1912. pp. 752–979.
6. Baker LA, Gomez RA. Embryonic development of the ureter. Semin Nephrol. 1998; 18: 569–584. PMID: 9819148.
7. Oliver J. Nephrons and kidneys; a quantitative study of developmental and evolutionary mammalian renal architectonics. New York: Hoeber Medical Division, Harper & Row; 1968.
8. Al-Awqati Q, Goldberg MR. Architectural patterns in branching morphogenesis in the kidney. Kidney Int. 1998; 54: 1832–1842. https://doi.org/10.1046/j.1523-1755.1998.00196.x PMID: 9853247.
9. Osathanondh V, Potter EL. Development of human kidney as shown by microdissection. II. Renal pelvis, calyces, and papillae. Arch Pathol 289. 1963; 76: 277–289. PMID: 14058155.
10. Shah MM, Sampogna RV, Sakurai H, Bush KT, Nigam SK. Branching morphogenesis and kidney disease. Development. 2004; 131: 1449–1462. https://doi.org/10.1242/dev.01089 PMID: 15023929.
11. Costantini F, Kopan R. Patterning a complex organ: Branching morphogenesis and nephron segmentation in kidney development. Dev Cell 712. 2010; 18: 698–712. https://doi.org/10.1016/j.devcel.2010.04.008 PMID: 20493806.
12. Ishiyama H, Ishikawa A, Kitazawa H, Fujii S, Matsubayashi J, Yamada S, et al. Branching morphogenesis of the urinary collecting system in the human embryonic metanephros. PLOS ONE. 2018; 13: e0203623. https://doi.org/10.1371/journal.pone.0203623 PMID: 30192900
13. Kitazawa H, Fujii S, Ishiyama H, Matsubayashi J, Ishikawa A, Yamada S, et al. Nascent nephrons during human embryonic development: Spatial distribution and relationship with urinary collecting system. J Anat. 2021; 238: 455–466. https://doi.org/10.1111/joa.13308 PMID: 32888205
14. Potter EL. Normal and abnormal development of the kidney. Chicago: Year Book Medical Publishers; 1972.
15. Lindström NO, McMahon JA, Guo J, Tran T, Guo Q, Rutledge E, et al. Conserved and divergent features of human and mouse kidney organogenesis. J Am Soc Nephrol. 2018; 29: 785–805. https://doi.org/10.1681/ASN.2017080887 PMID: 29449453
16. Newman J, Antonakopoulos GN. The fine structure of the human fetal urinary bladder. Development and maturation. A light, transmission and scanning electron microscopic study. J Anat. 1989; 166: 135–150. PMID: 2621133
17. Brace RA, Wolf EJ. Normal amniotic fluid volume changes throughout pregnancy. Am J Obstet Gynecol. 1989; 161: 382–388. https://doi.org/10.1016/0002-9378(89)90527-9 PMID: 2764058.
18. Yamaguchi Y, Yamada S. The Kyoto collection of human embryos and fetuses: History and recent advancements in modern methods. Cells Tissues Organs. 2018; 205: 314–319. https://doi.org/10.1159/000490672 PMID: 30064127
19. O'Rahilly R, Müller F. Developmental stages in human embryos: Including a revision of Streeter's Horizons and a survey of the Carnegie Collection. Washington: Carnegie Institution of Washington; 1987. p. 1 306.
20. Shuangshoti S, Netsky MG. Histogenesis of choroid plexus in man. Am J Anat. 1966; 118: 283–316. https://doi.org/10.1002/aja.1001180114 PMID: 5915034
21. Shiraishi N, Nakashima T, Yamada S, Uwabe C, Kose K, Takakuwa T. Morphogenesis of lateral choroid plexus during human embryonic period. Anat Rec (Hoboken). 2013; 296: 692–700. https://doi.org/10.1002/ar.22662 PMID: 23401483
22. Yamada M, Udagawa J, Hashimoto R, Matsumoto A, Hatta T, Otani H. Interkinetic nuclear migration during early development of midgut and ureteric epithelia. Anat Sci Int. 2013; 88: 31–37. https://doi.org/10.1007/s12565-012-0156-8 PMID: 23054939
23. Huff DS, Carreon CK. Gastrointestinal tract. In: Ernst L, Ruchelli E, Carreon C, Huff D, editors. Color atlas of human fetal and neonatal histology. Cham: Springer; 2019. https://doi.org/10.1007/978-3-030-11425-1_4

24. Signoretti S, Pires MM, Lindauer M, Horner JW, Grisanzio C, Dhar S, et al. p63 regulates commitment to the prostate cell lineage. Proc Natl Acad Sci U S A. 2005; 102: 11355–11360. [Epub 2005 Jul 28]. https://doi.org/10.1073/pnas.0500165102 PMID: 16051706.

25. Kreiger PA, Pogoriler JE. Lung. In: Ernst L, Ruchelli E, Carreon C, Huff D, editors. Color atlas of human fetal and neonatal histology. Cham: Springer; 2019. https://doi.org/10.1007/978-3-030-11425-1_3

26. Hashimoto K, Gross BG, Lever WF. The ultrastructure of human embryo skin. II. The formation of intradermal portion of the eccrine sweat duct and of the secretory segment during the first half of embryonic life. J Invest Dermatol. 1966; 46: 513–529. https://doi.org/10.1038/jid.1966.79 PMID: 25622419.

PLOS ONE

RESEARCH ARTICLE

# Femoral posture during embryonic and early fetal development: An analysis using landmarks on the cartilaginous skeletons of *ex vivo* human specimens

**Tetsuya Takakuwa[1]*, Marie Ange Saizonou[1], Sena Fujii[1], Yousuke Kumano[1], Aoi Ishikawa[1], Tomoki Aoyama[1], Hirohiko Imai[2], Shigehito Yamada[1,3], Toru Kanahashi[1]**

**1** Human Health Science, Graduate School of Medicine, Kyoto University, Kyoto, Japan, **2** Department of Systems Science, Graduate School of Informatics, Kyoto University, Kyoto, Japan, **3** Congenital Anomaly Research Center, Graduate School of Medicine, Kyoto University, Kyoto, Japan

* tez@hs.med.kyoto-u.ac.jp



OPEN ACCESS

**Citation:** Takakuwa T, Saizonou MA, Fujii S, Kumano Y, Ishikawa A, Aoyama T, et al. (2023) Femoral posture during embryonic and early fetal development: An analysis using landmarks on the cartilaginous skeletons of *ex vivo* human specimens. PLoS ONE 18(5): e0285190. https://doi.org/10.1371/journal.pone.0285190

**Editor:** Aliah Faisal Shaheen, Brunel University London, UNITED KINGDOM

**Received:** August 9, 2022

**Accepted:** April 17, 2023

**Published:** May 2, 2023



**Data Availability Statement:** All relevant data are within the manuscript and its Supporting Information files.

**Funding:** This study was supported by Grant No. 21K07772 and 20K22736 from the Japan Society for the Promotion of Science. The funders had no role in study design, data collection and analysis, decision to publish, or preparation of the manuscript.

## Abstract

The pre-axial border medially moves between the fetal and early postnatal periods, and the foot sole can be placed on the ground. Nonetheless, the precise timeline when this posture is achieved remains poorly understood. The hip joint is the most freely movable joint in the lower limbs and largely determines the lower-limb posture. The present study aimed to establish a timeline of lower-limb development using a precise measurement of femoral posture. Magnetic resonance images of 157 human embryonic samples (Carnegie stages [CS] 19–23) and 18 fetal samples (crown rump length: 37.2–225 mm) from the Kyoto Collection were obtained. Three-dimensional coordinates of eight selected landmarks in the lower limbs and pelvis were used to calculate the femoral posture. Hip flexion was approximately 14˚ at CS19 and gradually increased to approximately 65˚ at CS23; the flexion angle ranged from 90˚ to 120˚ during the fetal period. Hip joint abduction was approximately 78˚ at CS19 and gradually decreased to approximately 27˚ at CS23; the average angle was approximately 13˚ during the fetal period. Lateral rotation was greater than 90˚ at CS19 and CS21 and decreased to approximately 65˚ at CS23; the average angle was approximately 43˚ during the fetal period. During the embryonic period, three posture parameters (namely, flexion, abduction, and lateral rotation of the hip) were linearly correlated with each other, suggesting that the femoral posture at each stage was three-dimensionally constant and exhibited gradual and smooth change according to growth. During the fetal period, these parameters varied among individuals, with no obvious trend. Our study has merits in that lengths and angles were measured on anatomical landmarks of the skeletal system. Our obtained data may contribute to understanding development from anatomical aspects and provide valuable insights for clinical application.

**Competing interests:** The authors have declared that no competing interests exist.

## 1. Introduction

The Carnegie staging system categorizes the first eight weeks after fertilization into 23 stages and is widely used [1, 2]. Staging is based on external appearance and internal findings. Because limb development is a conspicuous and potentially helpful marker for the identification of normal development, the staging system therefore includes limb findings. The upper-limb bud emerging at Carnegie stage (CS) 12 is the first externally detectable finding during human development [1, 2]. The lower-limb bud subsequently appears following the emergence of the upper-limb bud, with a lag of one or two stages (i.e., at CS13 or CS14). Until CS19, the axes of both the upper and lower limbs are more or less parallel. Pre-axial and post-axial borders can be identified, which are cephalic and caudal to the longitudinal axis, respectively. The future thumb and big toe are located on the pre-axial border of the hand and footplates, respectively.

The pre-axial border medially moves between the fetal and early postnatal periods, and the foot sole can be placed on the ground [3]. Several anatomical structures observed in adult lower limbs indicate the medial rotation of the lower limbs during development. For instance, the segmental pattern of lower-limb innervation twists into a spiral [2], and three capsular ligaments (namely, the iliac, pubic, and ischiofemoral ligaments) around the hip joint run spirally [4]. In symmelia, the post-axial side, including the fibula, merges medially. Considering that symmelia becomes visible prior to the end of the embryonic period (i.e., CS23), medial rotation is thought to begin during the embryonic period [3, 5]. Nonetheless, the precise timeline during which this posture is achieved remains poorly understood.

O'Rahilly and Gardner estimated the lower-limb rotation using toe and foot orientations as reference points; they described that the hallux was located on the cranial side and that the foot sole oriented medially at CS23 [3], which is referred to as the famous "praying feet" posture (Fig 1). Thus, they considered that the pre-axial border remained cranial at the end of the embryonic period (i.e., CS23). During the late embryonic and early fetal periods, the limbs markedly increase in length and exhibit more advanced differentiation in their subdivisions [6, 7]. The hip, knees, ankle joints, and pelvis may contribute to the lower-limb posture. With respect to the ankle joints, physiological clubfoot is recognized during the embryonic and early fetal periods [8, 9]. Physiological clubfoot is a decrease in the foot angle with the frontal side of the leg (plantar flexion), as well as an increase in the foot angle initially, followed by a subsequent decrease in the foot angle with the lateral side of the leg (adduction) (Fig 1). Therefore, the methods of O'Rahilly and Gardner [3] for estimating the timeline of lower-limb rotation seem inappropriate.

There has been remarkable progress in the visualization of the developing fetus owing to recent developments in three-dimensional (3D) sonographic imaging techniques [8, 10, 11]. The use of *in vivo* images (e.g., 3D/4D ultrasound images) may be realistic and ideal because they can enable the visualization of the embryonic and fetal posture in the physiological intrauterine environment, as well as the monitoring of the growth and differentiation of the same individuals. However, during the embryonic period, the cartilaginous skeleton is less echogenic, and accurate identification and quantitative measurement of the posture are challenging to accomplish.

Among anatomical structures, the hip joint is the most freely movable in the lower limbs and largely determines the lower-limb posture. No previous studies provided sufficient knowledge about the femoral posture during the embryonic and early fetal period. Hence, the present study aimed to establish a timeline of lower-limb development using a precise measurement of femoral posture. We successfully achieved this by evaluating the 3D position of the femur relative to the body axis (sacrum) using anatomical landmarks on the lower-limb joints.

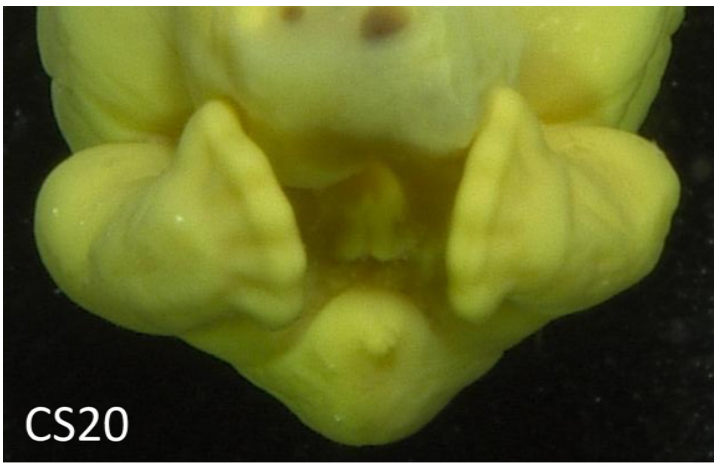
CS20

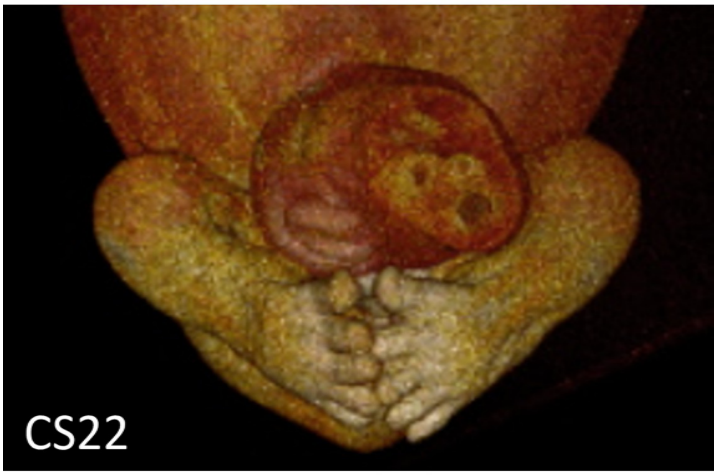
CS22

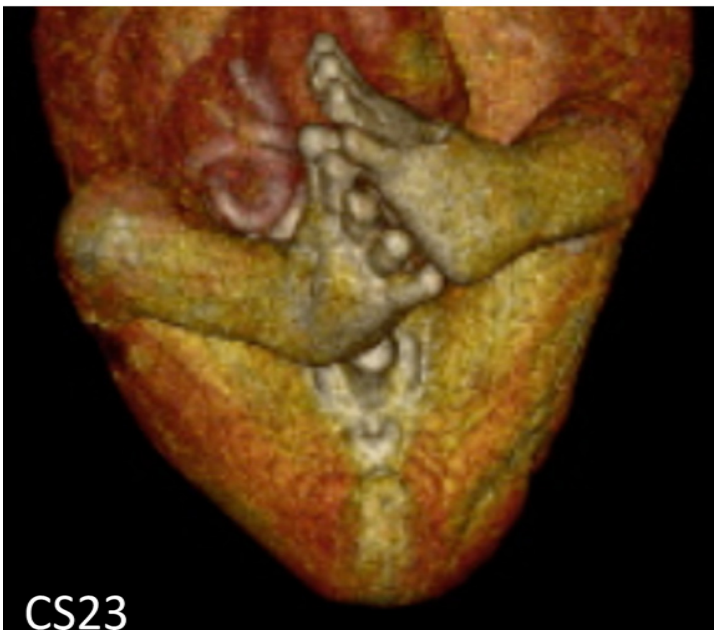
CS23

**Fig 1. Representative ventral image showing the lower-limb posture during the late embryonic period.** Note that the impressive "praying feet" posture (i.e., the hallux was located on the cranial side, and the foot sole oriented medially) was observed at CS23 or earlier stages. The hip joint showed <90˚ of lateral rotation, whereas the ankle showed adduction. Abbreviation: CS, Carnegie stage.

https://doi.org/10.1371/journal.pone.0285190.g001

## 2. Materials and methods

### 2.1. Human embryonic specimens

The ethics committee of Kyoto University Faculty and Graduate School of Medicine approved this study (E986 and R0316), which used human embryonic and fetal specimens.

The samples included 157 human embryonic specimens between CS19 and CS23 (CS19; N = 25, CS20; N = 38, CS21; N = 36, CS22; N = 32, and CS23; N = 26) and 18 fetal specimens (crown rump length [CRL]: 37–225 mm) from the Kyoto Collection at the Congenital Anomaly Research Center of Kyoto University, Japan [12]. The majority of specimens in the Kyoto Collection are stored for research purposes and provided on request; such specimens are acquired when a pregnancy is terminated for socioeconomic reasons under the Maternity Protection Law of Japan. Samples were collected between 1963 and 1995 in accordance with the relevant regulations during these time periods. Written informed consent from parents was not required at that time; instead, the parents provided verbal informed consent for the deposition of specimens, and consent was documented in medical records. All samples were anonymized and de-identified. Approximately 20% of these fetal specimens are undamaged and well-preserved. Specimens of aborted fetuses were brought to the laboratory, where they were measured, examined, and staged using the criteria proposed by O'Rahilly and Müller in 1987 [1]. Staging of the embryos used was performed by TT (author) and Ms. Chigako Uwabe (acknowledged for technical assistance).

### 2.2. Magnetic resonance image processing and selection of datasets

Magnetic resonance imaging (MRI) was performed using a 2.35-T MRI system [13], 7-T MRI system (BioSpec 70/20 USR; Bruker BioSpin MRI GmbH, Ettlingen, Germany), and a 3-T MRI system (MAGNETOM Prisma; Siemens Healthineers, Erlangen, Germany). The image acquisition method was selected according to the desired specimen resolution and volume. The 2.35-T MRI system was used to acquire 3D images of all embryonic samples between CS19 and CS23 [13, 14]. The 7-T MRI system was used to acquire 3D images of fetal specimens with a CRL of 37.2–103 mm, whereas the 3-T MRI system was utilized to obtain 3D images of fetal samples with a CRL of >116 mm. The conditions for acquisition are described elsewhere [15].

In the present study, 3D images of the whole body were automatically obtained, whereas 3D images of the pelvis and femur were manually reconstructed using AMIRA software version (Visage Imaging GmbH, Berlin, Germany).

### 2.3. Definition of landmarks, 3D axis, and measurements

For embryonic specimens, 3D coordinates were initially assigned to eight selected landmarks by examining the voxel's position on 2D sequential images and 3D images using Miele-LXIV (Alex Bettarini, https://dicom.3utilities.com/) or AMIRA software (Fig 2). The eight selected landmarks were as follows: center of bilateral femoral heads (H_r, H_l); bilateral knee (K_r, K_l) and ankle joints (A_r, A_l); and cranial region of the first and third sacral vertebrae (S1, S3). For fetal specimens, the medial and lateral femoral epicondyles (Me_r, Me_l, Le_r, Le_l) were selected instead of the bilateral ankle joints.

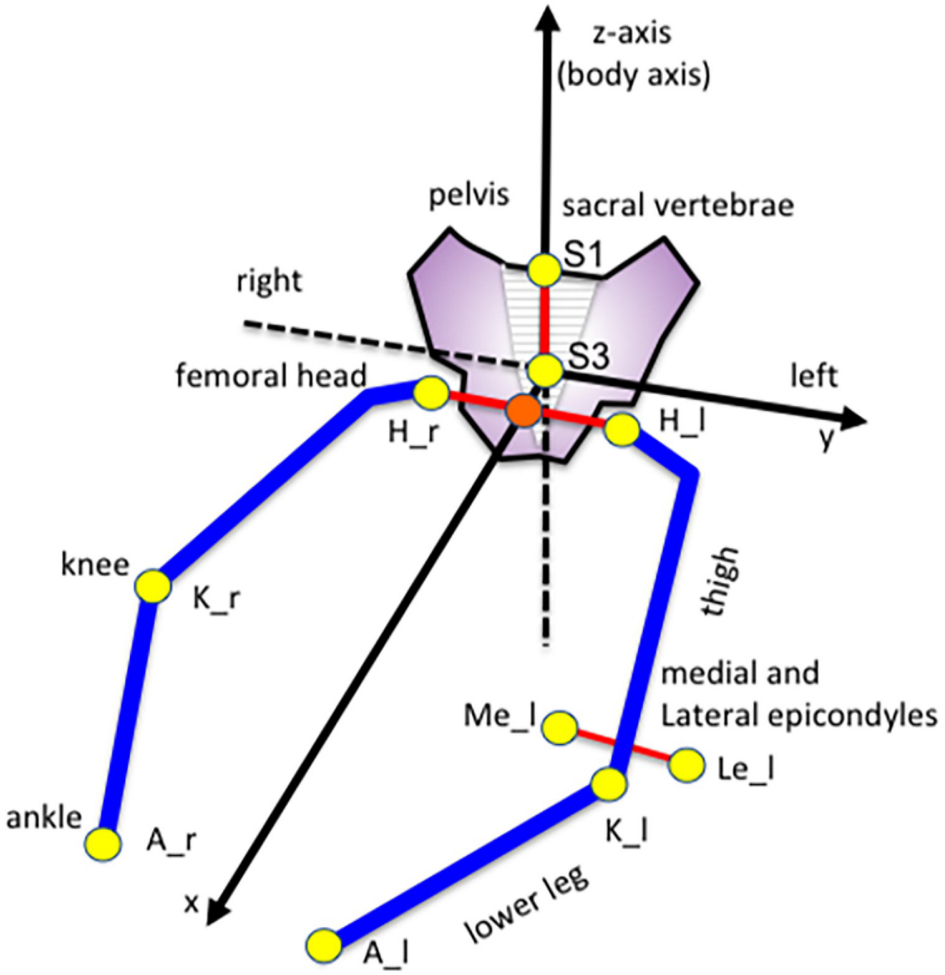


**Fig 2. Definitions of the landmarks and coordinate system.** For embryonic specimens, the eight selected landmarks were as follows: center of bilateral femoral heads (H_r, H_l); bilateral knee (K_r, K_l) and ankle joints (A_r, A_l); and cranial region of the first and third sacral vertebrae (S1, S3). For fetal specimens, the medial and lateral femoral epicondyles (Me_r, Me_l, Le_r, Le_l) were selected instead of the bilateral ankle joints. S3 was defined as the origin and the z-axis (body axis) as the line through S1 and S3. The z–x plane (median plane) was defined using the midpoint between H_l and H_r (H_m); H_m was located in the median plane. The y-axis was defined as the normal vector of the median plane, and the x-axis was calculated as the outer product of the z- and y-axes.

https://doi.org/10.1371/journal.pone.0285190.g002

The original coordinate values were translated into another coordinate system, in which S3 was defined as the origin and the z-axis (body axis) as the line through S1 and S3 (Fig 2). The z–x plane (median plane) was defined using the midpoint between H_l and H_r (H_m); H_m was located in the median plane. The y-axis was defined as the normal vector of the median plane, and the x-axis was calculated as the outer product of the z- and y-axes. Two of the authors (MAS and AI) independently acquired the 3D reconstructions and landmarks. When landmark values were missing or apparently different between two observers, the data were re-acquired. The samples were excluded if the re-acquired data were still discrepant. Consequently, 15 embryonic samples and one fetal sample were excluded from further analysis. The remaining samples had no missing data. Measurements were highly reproducible (intra-class correlation coefficient: 0.90<). The average value for each specimen was used in this study.

The lengths of the bilateral femoral shafts (segments HK_r and HK_l), lower leg (segments KA_r and KA_l), inter-hip joint (segment H_r-H_l), and inter-sacrum S1–S3 were calculated.

The right femoral posture relative to the body axis was defined as the angle between segment HK_r and the z-axis, whereas the left femoral posture was defined as the angle between segment HK_l and the z-axis. These angles were projected onto the median and coronal planes to obtain the flexion and abduction angles. For embryonic samples, the lateral rotation angle of the right femur was calculated using the z-axis, segment HK_r, and vector of plane HKA_r, whereas the lateral rotation angle of the left femur was calculated using the z-axis, segment HK_l, and vector of plane HKA_l. As for the lateral rotation angle for fetal samples, the vector Le-Me was used instead of the vector of plane HKA.

Knee flexion was calculated as the angle between HK_r and KA_r and between HK_l and KA_r. The angle between H_r-S1 and S1-H_l was projected onto the x–y plane (i.e., transverse plane) and was defined as the hip–sacrum angle. The height of the hip joint along the z-axis was calculated by comparing the S1–S3 length. All length and angle values obtained were provided in S1 Datasets.

## 3. Results

### 3.1. Femoral posture

**3.1.1. Lateral view (hip and knee flexion).** The femur was elongated caudally, as shown in Fig 3. Hip flexion was approximately 14˚ at CS19 and gradually increased during the embryonic period, reaching approximately 65˚ at CS23 (Fig 4A). During the fetal period, the thigh was in the "sitting position," and morphometry indicated that hip flexion increased to 107˚. The hip flexion angle in most samples ranged from 90˚ to 120˚, which was relatively constant, as compared to the hip rotation angle. Knee flexion was approximately 70˚ at CS19 and gradually increased to approximately 90˚ at CS23 (Fig 4B).

**3.1.2. Ventral view (abduction and lateral rotation).** The hip joint showed abduction from the z-axis during the embryonic period (Fig 5). Abduction at the hip joint was approximately 78˚ at CS19 and gradually decreased to approximately 27˚ at CS23 (Fig 6A). The average angle during the fetal period was 10.1˚ on the right and 15.5˚ on the left. The angle ranged from 0˚ to 30˚, which was relatively constant, as compared with the hip rotation angle. The angle measures were diverse among the samples.

At CS19 and CS21, the greater trochanter was located on the caudal side and was recognizable in the ventral view (asterisk in Fig 5), suggesting that the femur showed lateral rotation. Morphometry revealed that lateral rotation was greater than 90˚ at CS19 and CS21 and decreased to approximately 65˚ at CS23 (Fig 6B). The average angle during the fetal period was 39.6˚ on the right and 46.8˚ on the left. The angle measures were diverse among the samples.

**3.1.3. Comparison of three posture parameters.** Three posture parameters—namely, flexion, abduction, and lateral rotation of the hip—were linearly correlated with each other at CS19 and later stages (Fig 7). The coefficient of determination ($R^2$) was 0.96 and 0.90 for right and left flexion vs. abduction, 0.92 and 0.85 for right and left flexion vs. lateral rotation, and 0.90 and 0.83 for right and left abduction vs. lateral rotation, respectively.

### 3.2. Pelvic ring formation and length measurements

Prior to pelvic ring formation, the pelvis was "platypelloid." Consequently, the hip–sacrum angle changed (Fig 8A). The angle was >100˚ at CS19 and CS21 but decreased to 87˚ at CS23 and then 82˚ during the fetal period (Fig 8B). This angle had a relatively narrow range in most fetal specimens (75˚ to 85˚).

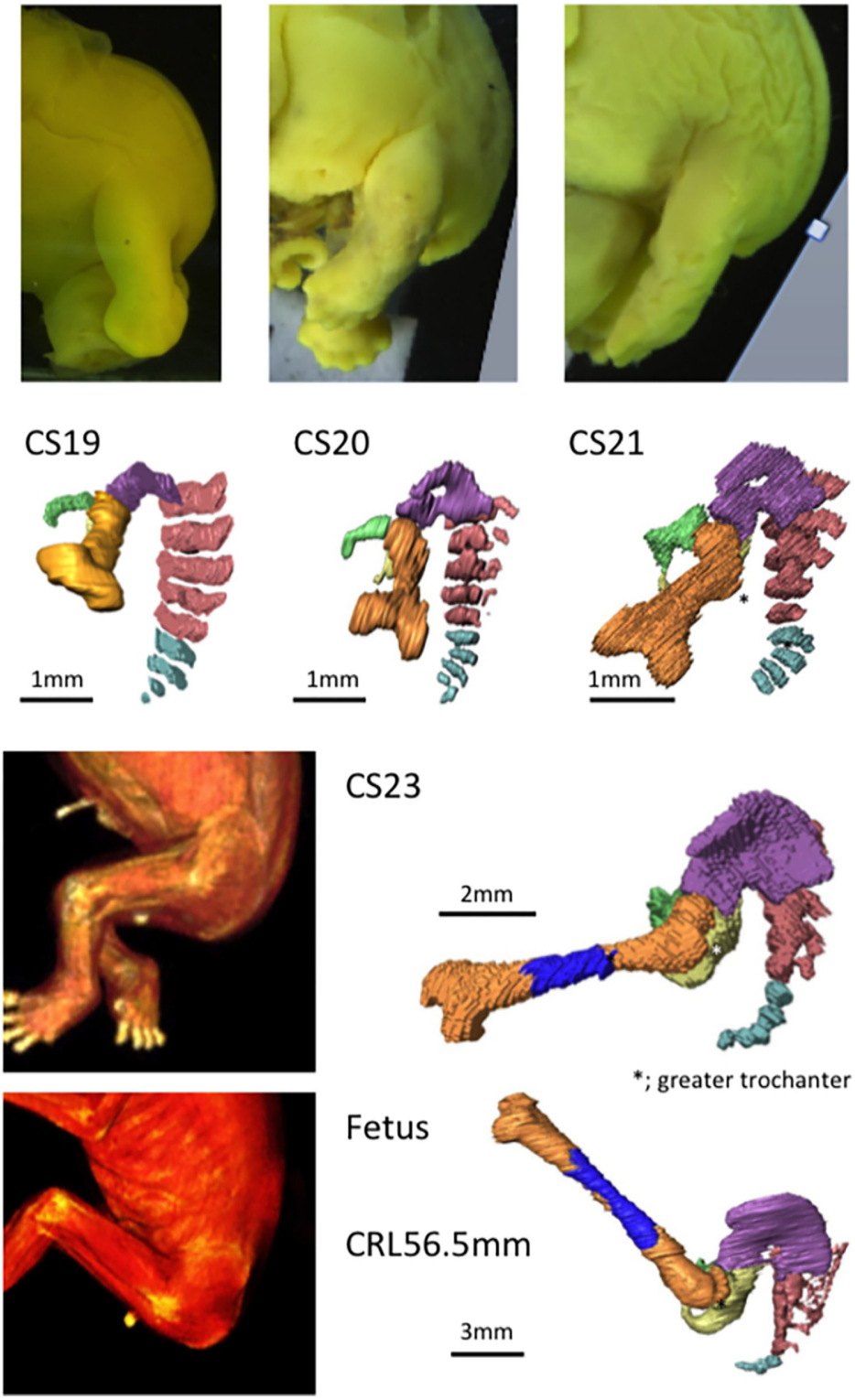


**Fig 3. Representative overall pictures and 3D reconstructions of skeletal structures: The hip joint (lateral view) during the embryonic period between CS19 and CS23 and during the early fetal period.** Note that the relative position of the hip joint and sacrum in the cranial–caudal direction changed between the embryonic and fetal periods. Legends: blue, femur (ossified); brown, femur (not ossified); green, pubis; light blue, coccyx; pink, sacrum; purple, ilium; yellow, ischium. "*" indicates the greater trochanter.

https://doi.org/10.1371/journal.pone.0285190.g003

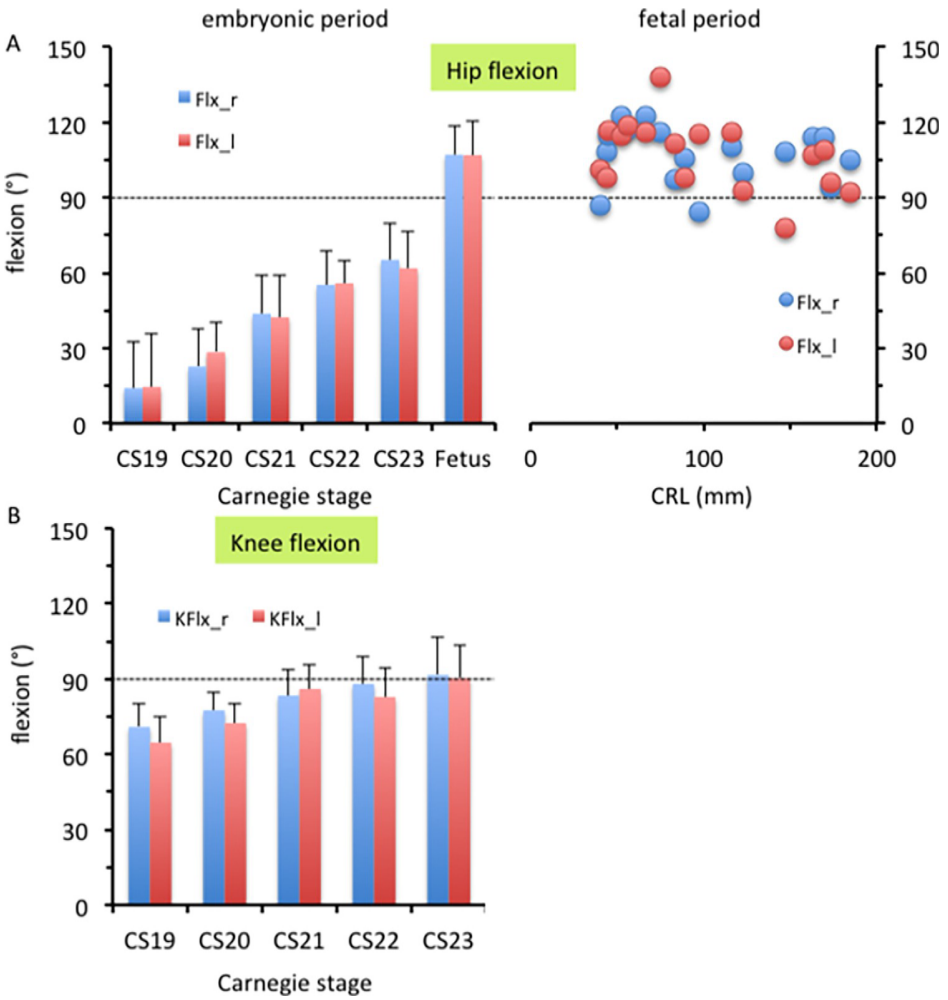


**Fig 4. Flexion angle in the lower limbs.** Hip joint (A) and knee joint (B) flexion. (A) Hip joint flexion during the embryonic (left) and fetal (right) periods. (B) Knee joint flexion during the embryonic period. Legends: blue, right lower limb; red, left lower limb.

https://doi.org/10.1371/journal.pone.0285190.g004

The relative position of the hip joint and sacrum in the cranial–caudal direction was noted to have changed between the embryonic and fetal periods (Fig 8C). The hip joint was located almost at the level of S1 during the embryonic period and at the level of S3 during the fetal period (see also Fig 3).

The inter-hip joint length was almost constant (0.33–0.37 mm) from CS19 to CS22, as compared with other length measurements such as S1–S3 length, femoral shaft length, and lower-leg length (Fig 9). During the fetal period, all length measurements linearly increased according to growth.

As indicated by the ventral (Fig 5) and cranial views (Fig 8A), the pelvic ring was still open at CS19; subsequently, it was closed by sacroiliac joint formation at CS21 and pubic symphysis formation at CS23.

## 4. Discussion

The present study evaluated the femoral posture using the angle between the z-axis (body axis) and the line on the hip and knee joints. The planes of the hip, knee, and ankle joints were used

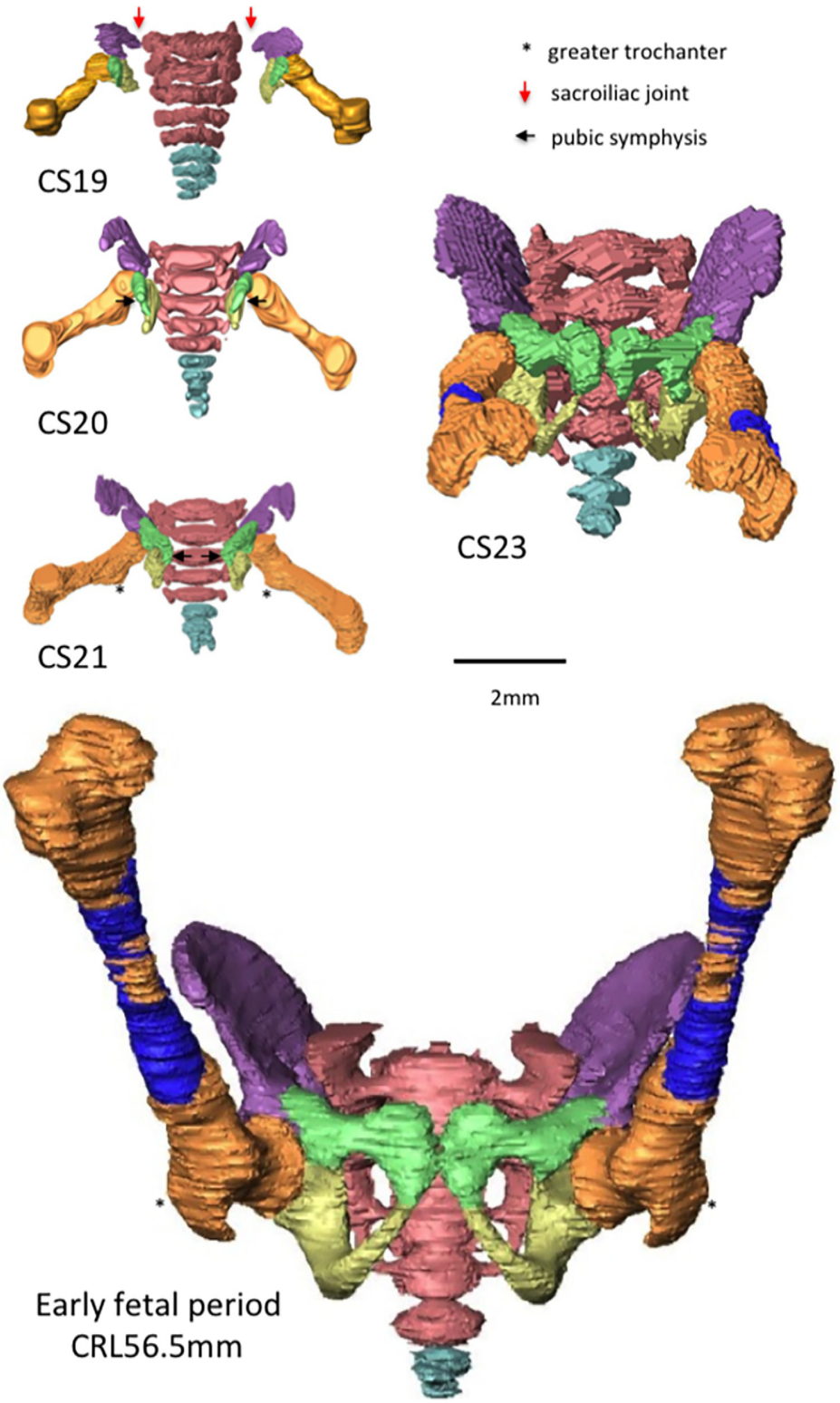


**Fig 5. Representative 3D reconstructions of skeletal structures: The hip joint (ventral view).** Note that the pubic symphysis (black arrows) was first contacted at CS23. Legends: blue, femur (ossified); brown, femur (not ossified); green, pubis; light blue, coccyx; pink, sacrum; purple, ilium; yellow, ischium. "*" indicates the greater trochanter, and the red arrows point at the sacroiliac joint.

https://doi.org/10.1371/journal.pone.0285190.g005

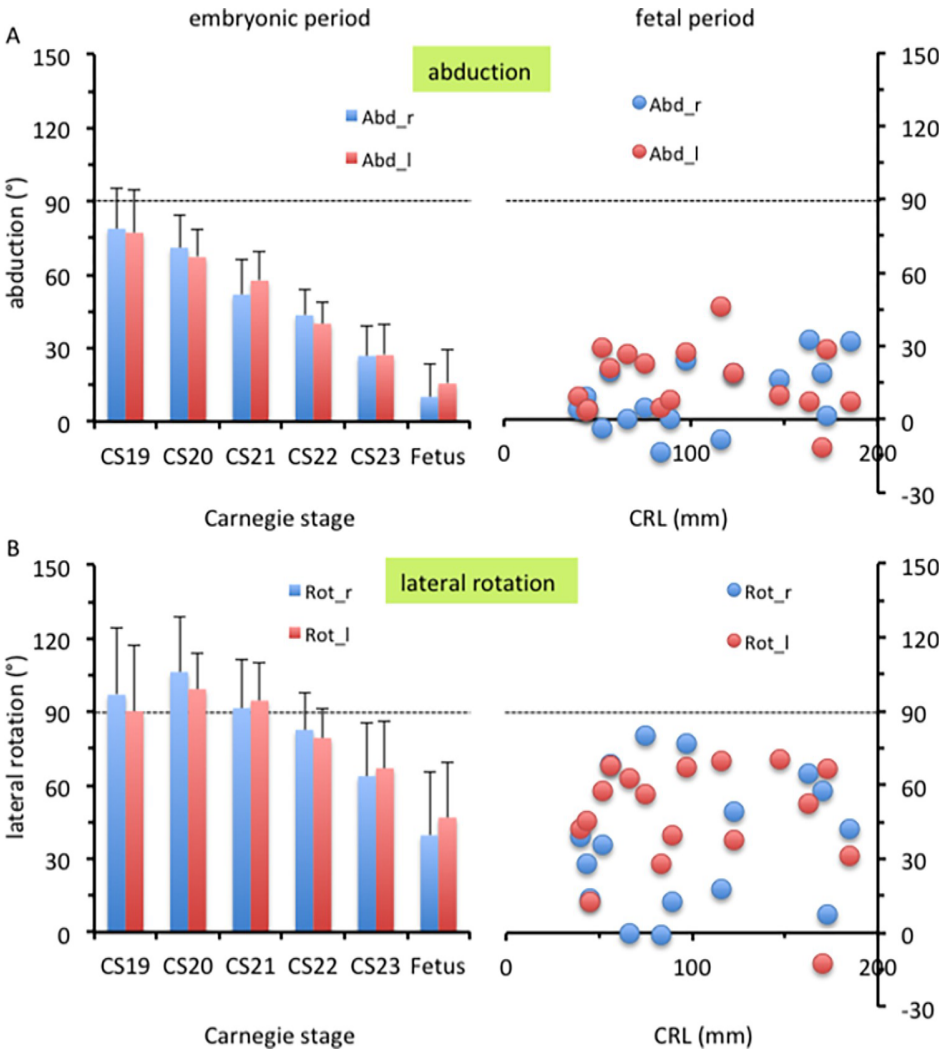


**Fig 6. Abduction angle and lateral rotation angle of the hip.** (A) Abduction angle of the hip during the embryonic (left) and fetal (right) periods. (B) Lateral rotation angle of the hip during the embryonic (left) and fetal (right) periods.

https://doi.org/10.1371/journal.pone.0285190.g006

to evaluate lateral rotation, as abduction and adduction of the knee joint might be limited. Our hip joint angle calculation for the evaluation of lower-limb posture is more accurate than that applied in a previous study [3], in which toe and foot orientations were used as reference points.

Changes in lateral rotation, adduction, and flexion during the embryonic period were -37.4˚, -51˚, and 49.2˚, respectively. Our results were inconsistent with the description in several textbooks that 90˚ rotation occurs at eight weeks of gestation [16–19]. O'Rahilly and Gardner [3] reported that the pre-axial border remained cranial at the end of the embryonic period proper (CS23), on the basis that the big toe was located on the cranial side and the foot sole was oriented medially at CS23. It should be noted that the lower-limb structure of an embryo or fetus is different from that of an adult. For instance, the "physiological clubfoot" is recognized during the embryonic and early fetal periods (Fig 1) [8, 9]; therefore, the foot's orientation should not be used as an indicator of lower-limb posture.

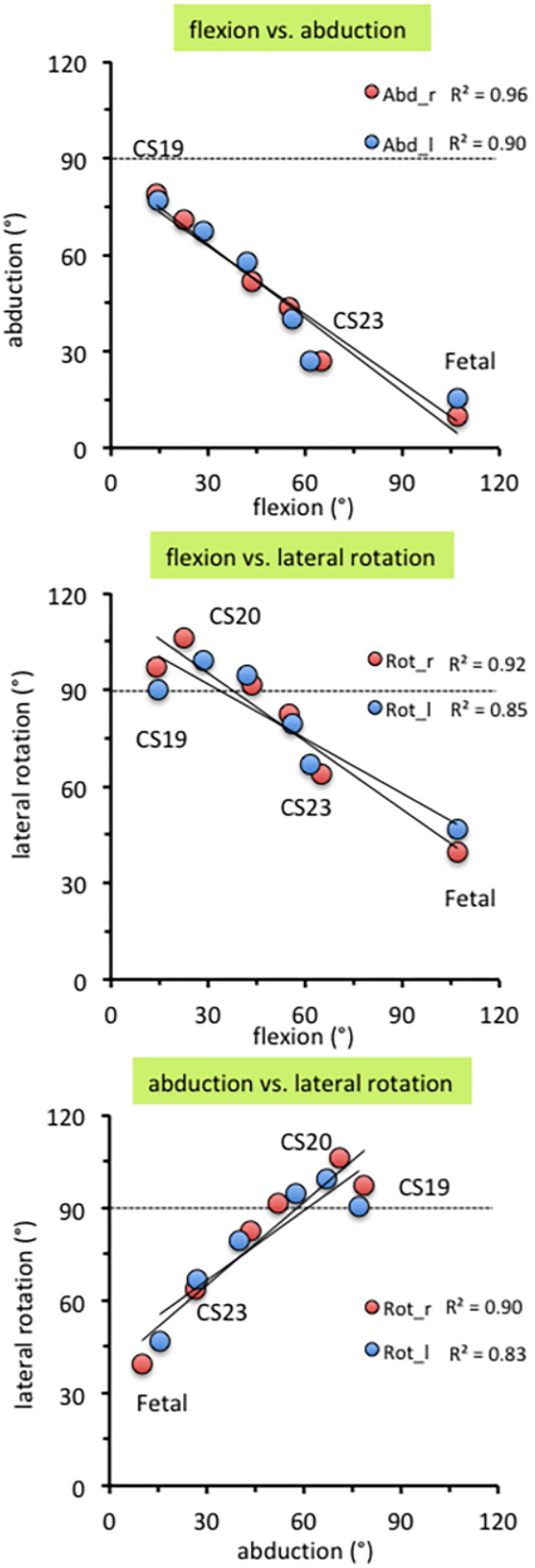


**Fig 7. Correlation between flexion, abduction, and lateral rotation of the hip.**

https://doi.org/10.1371/journal.pone.0285190.g007

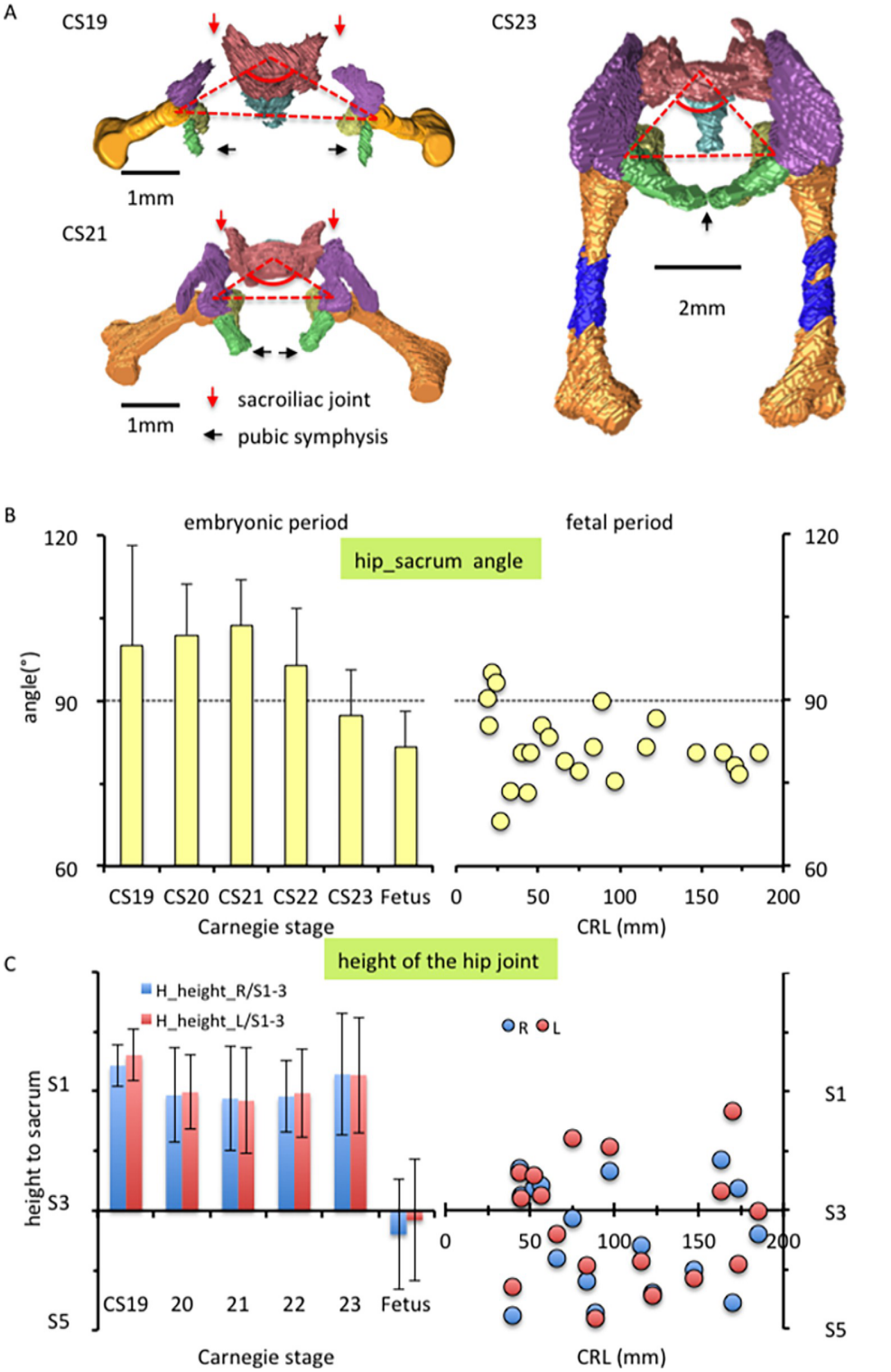


**Fig 8. Pelvic ring formation.** (A) Cranial view of the 3D reconstruction indicating pelvic ring formation during the embryonic period (CS19, CS21, and CS23). The red triangle indicates the hip–sacrum angle (i.e., the angle between the right femoral head, first sacrum, and left femoral head [∠H_r-S1 and S1-H_l]), which was projected onto the x–y plane (transverse plane). Legends: Blue, femur (ossified); brown, femur (not ossified); green, pubis; light blue, coccyx; pink,

sacrum; purple, ilium; yellow, ischium. (B) Change in the hip–sacrum angle during the embryonic (left) and fetal (right) periods. (C) Height of the hip joint during the embryonic (left) and fetal (right) periods. The height of the hip joint along the z-axis (cranial–caudal direction) is shown, with the position of S3 indicated as a reference.

https://doi.org/10.1371/journal.pone.0285190.g008

Three posture parameters—namely, flexion, abduction, and lateral rotation of the hip—were linearly correlated with each other during the embryonic period, suggesting that the femoral posture at each stage was three-dimensionally constant and gradually and smoothly changed according to growth. During the fetal period, these posture parameters varied among individuals, especially the lateral hip rotation angle. No obvious trend in this variation was observed. When the joint cavity develops and a pelvic ring structure is formed during the fetal

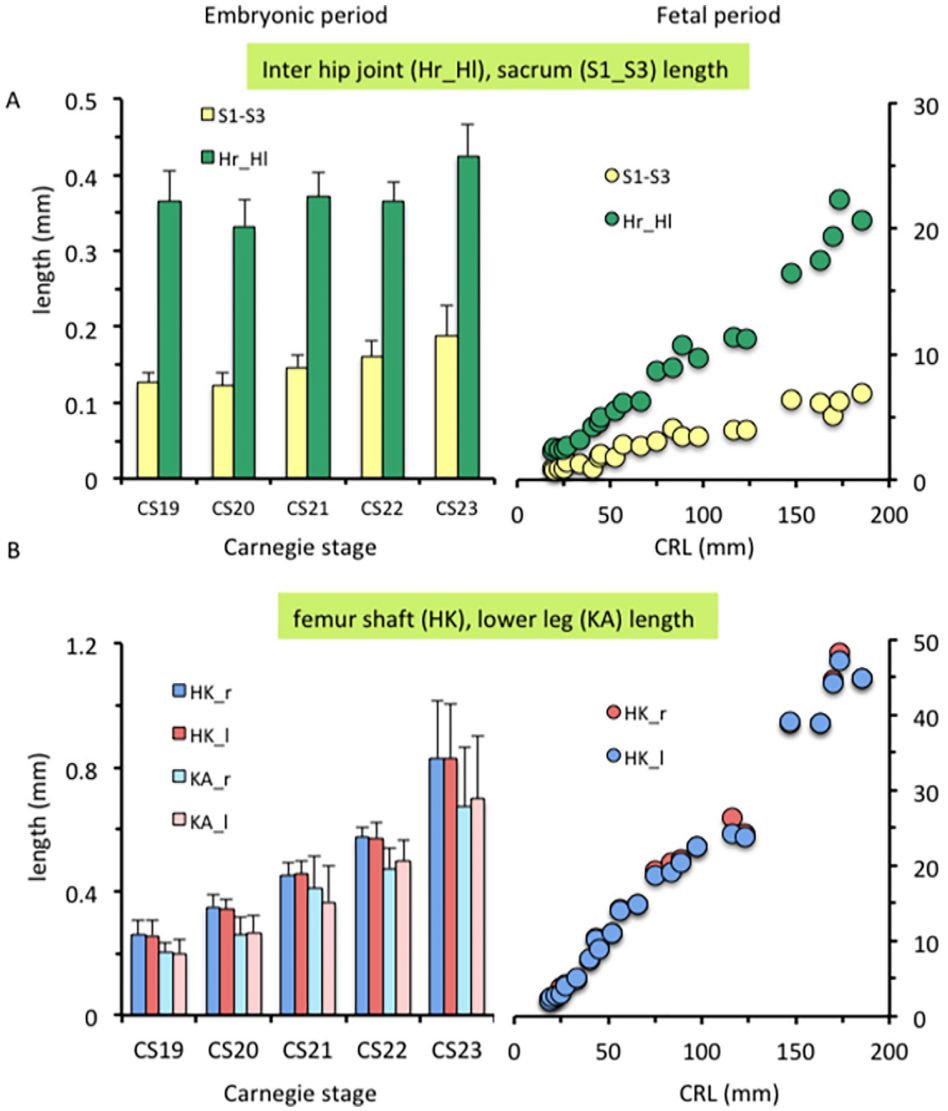


**Fig 9. Length measurements of the lower limbs.** (A) Pelvic length measurements during the embryonic (left) and fetal (right) periods: lengths of the inter-hip joint (segment H_r-H_l) and sacrum (S1–S3). (B) Length measurements of the lower limbs during the embryonic (left) and fetal (right) periods: lengths of the bilateral femoral shafts (segment H-K) and lower limbs (segment K-A).

https://doi.org/10.1371/journal.pone.0285190.g009

period, the hip joint may be actively movable in the uterus. Thus, the posture of the preserved fetal samples might not accurately reflect the intrauterine posture.

We recently presented data on upper-arm posture [15], as well as the morphogenesis and position of the scapula [20]. There were similarities in posture between the upper arms and thighs, as described in the present study. A gradual change in posture was observed during the embryonic period, in which the maximum value was attained at CS19 or CS20; in contrast, the posture was relatively constant during the fetal period. For both upper and lower limbs, individual differences were large during the fetal period. With respect to the abovementioned three parameters, a decrease in abduction was observed in both upper and lower limbs. Unfortunately, this gradual change in posture may be unsuitable as a parameter for staging, which requires a specific form in appearance.

On the other hand, the following differences in posture were observed between the upper and lower limbs. Decreased lateral rotation was evident in the lower limbs but was inconspicuous in the upper limbs. As for flexion, the angle in the lower limbs increased during the embryonic period and was constantly high during the fetal period, whereas the angle in the upper limbs was relatively constant (45˚ to 90˚). It should be noted that the position of the scapula influences the upper-arm posture. The position of the scapula considerably changed and was significantly different between the embryonic and fetal periods. Abduction and flexion of the scapulothoracic articulation were significantly increased, which affected the upper-limb posture. Regarding the lower limbs, the sacropelvic joint was formed at CS21 and the pubic symphysis was observed at CS23 (Figs 5 and 8A). Pelvic ring formation may influence the abduction angle in the lower limbs; nevertheless, such influence may be less than the influence of the scapula on the upper-limb posture. However, in the present study, we could not clarify the effect of pelvic ring formation on the lower-limb posture.

The hip joint consists of the femoral head and pelvis. The pelvis and femur are connected, and the border can be recognized in samples through the presence of dense mesenchymal cells at CS21 and earlier stages. Although they are still connected, the density of mesenchymal cells decreases between CS22 and CS23. The Y-shaped connection of the three parts of the hip bone (namely, the ischium, pubis, and ilium) forms the acetabulum at approximately CS23 [6, 21, 22]. A previous study reported that cavitation was initiated in samples with a CRL of $\geq$30 mm and was always observed in samples with a CRL of $\geq$56 mm [6]. Changes in the hip joint posture during the embryonic period may cause considerable stress on the musculoskeletal system of the hip joint, considering that the pelvis and femur are connected. Future studies should investigate the effects of stress on this system.

The trochanter initially forms at approximately CS21, and the femoral neck–shaft angle is observed at the end of the embryonic period. The angle ranges from approximately 135˚ to 145˚ before femoral ossification (from CS23 to the early fetal period) and is approximately 130˚ during the fetal period, which is similar to that in adults [7]. Furthermore, the detected anteversion angle is approximately 25˚ before ossification and ranges from 10˚ to 20˚ during the fetal period. These angles can potentially influence each other in a complex manner. Ideally, the angle should be measured at the femoral shaft and neck separately. However, in the present study, setting the proper landmarks on the trochanter to accurately separate the femoral neck and shaft was difficult to accomplish because of the low MRI resolution and trochanter's immature form during the embryonic period.

Using 3D ultrasound in virtual reality, Bogers et al. recently analyzed the physiological development of the fetal foot position "physiological clubfoot" during the first trimester [9]. Their study pointed out several issues for the applicability of their angle measurement technique to an embryonic study in the first trimester. The skeletal system during the embryonic period mainly comprises cartilages, which are less echogenic, and the lengths of the

cartilaginous fibula and tibia could not be measured in their study. Limb posture measurements depend on the surface view, which may reduce the accuracy. The success rate of angle measurements are still low (13.5–25.7%) for embryos at 8–9 weeks of gestational age. We consider that the hip joint will be much more difficult to accurately estimate using *in vivo* ultrasound images. The proportion of the trunk and thighs, which are not so long in the cranial–caudal direction, will not be suitable for accurate measurements of the hip joint length and angle if the skeletal system is not detected. In our opinion, accurate limb measurements using ultrasound images may be applicable during the fetal period when the body size becomes large, the limbs elongate longitudinally, and the bone structure begins to be detected.

The use of high-resolution MRI provides images of early anatomical development to improve the understanding of lower leg posture during the embryonic and early fetal period. This study also evaluates imaging data using the Carnegie collection [23] and expands on results from previous studies [1, 3]. Dawood et al. [24] highlighted the importance of ex utero imaging techniques, such as micro-CT and high-resolution MRI, to facilitate proper annotation of fetal structures in ultrasound scans of early first-trimester embryos and to improve detection of congenital anomalies in the developing embryo. From this point of view, our present study may help address these concerns and contribute to the improvement of the prenatal medicine.

### 4.1. Limitations

This study has some limitations. First, deformities and shrinkage due to fixation and preservation should be considered, as these may affect the limb posture, particularly in fetal samples after the formation of hip joint cavitation and pelvic ring. Second, although our samples were classified as normal based on external morphology, we could not unequivocally ascertained that all samples underwent normal development. Finally, staging between CS19 and CS23 was considerably difficult; however, we carefully staged the embryonic period samples, as previously described.

### 4.2. Conclusions

The angle calculation in our present study is more accurate than previous measures; hence, evaluating the femoral posture through our method is more reliable, revealing the precise timeline of femoral posture changes. The femoral posture at each embryonic stage was three-dimensionally constant and changed gradually and smoothly according to growth. The findings of our study may be difficult to apply clinically, however, our study has merits in that lengths and angles were measured on anatomical landmarks of the skeletal system. Our obtained data may contribute to an understanding about development from anatomical aspects and provide valuable insights for clinical application.

## Supporting information

**S1 Datasets. Length and angle values.**
(XLSX)

## Acknowledgments

The authors thank Ms. Chigako Uwabe for her technical assistance in handling the human embryos at the Congenital Anomaly Research Center of Kyoto University. The authors also thank Editage (www.editage.com) for English language editing.

## Author Contributions

**Conceptualization:** Tetsuya Takakuwa, Aoi Ishikawa.

**Data curation:** Toru Kanahashi.

**Formal analysis:** Marie Ange Saizonou, Sena Fujii, Yousuke Kumano.

**Funding acquisition:** Tetsuya Takakuwa.

**Project administration:** Tetsuya Takakuwa.

**Resources:** Hirohiko Imai, Shigehito Yamada.

**Software:** Sena Fujii.

**Validation:** Tomoki Aoyama.

**Visualization:** Toru Kanahashi.

**Writing – original draft:** Tetsuya Takakuwa.

## References

1. O'Rahilly R, Müller F. Developmental stages in human embryos: Including a revision of Streeter's "Horizons" and a survey of the Carnegie collection. Washington District of Columbia: Carnegie Institution of Washington; 1987.
2. O'Rahilly R, Müller F. Chapter 18. The skeletal system and limbs. In: O'Rahilly R, Müller F, editors. Human embryology and teratology. 3rd ed. New York: Wiley-Liss, Inc.; 2001. pp. 357–394.
3. O'Rahilly R, Gardner E. The timing and sequence of events in the development of the limbs in the human embryo. Anat Embryol (Berl). 1975; 148:1–23. https://doi.org/10.1007/BF00315559 PMID: 1202989
4. Standring S. Gray's anatomy. 41st ed. Amsterdam: Elsevier; 2005.
5. O'Rahilly R. Morphological patterns in limb deficiencies and duplications. Am J Anat. 1951; 89:135–193. https://doi.org/10.1002/aja.1000890202 PMID: 14894439
6. Okumura M, Ishikawa A, Aoyama T, Yamada S, Uwabe C, Imai H, et al. Cartilage formation in the pelvic skeleton during the embryonic and early-fetal period. PLoS One. 2017; 12:e0173852. https://doi.org/10.1371/journal.pone.0173852 PMID: 28384153
7. Suzuki Y, Matsubayashi J, Ji X, Yamada S, Yoneyama A, Imai H, et al. Morphogenesis of the femur at different stages of normal human development. PLoS One. 2019; 14:e0221569. https://doi.org/10.1371/journal.pone.0221569 PMID: 31442281
8. Victoria-Diaz A, Victoria-Diaz J. Pathogenesis of idiopathic clubfoot. Clin Orthop Relat Res. 1984; 185:14–24. PMID: 6705371
9. Bogers H, Rifouna MS, Cohen-Overbeek TE, Koning AHJ, Willemsen SP, et al. First trimester physiological development of the fetal foot position using three-dimensional ultrasound in virtual reality. J Obstet Gynaecol Res. 2019; 45:280–288. https://doi.org/10.1111/jog.13862 PMID: 30450690
10. Baken L, van Heesch PN, Wildschut HI, Koning AH, van der Spek PJ, Steegers EA, et al. First-trimester crown-rump length and embryonic volume of aneuploid fetuses measured in virtual reality. Ultrasound Obstet Gynecol. 2013; 41:521–525. https://doi.org/10.1002/uog.12365 PMID: 23225608
11. Baken L, van Gruting IM, Steegers EA, van der Spek PJ, Exalto N, Koning AH. Design and validation of a 3D virtual reality desktop system for sonographic length and volume measurements in early pregnancy evaluation. J Clin Ultrasound. 2015; 43:164–170. https://doi.org/10.1002/jcu.22207 PMID: 25041997
12. Yamaguchi Y, Yamada S. The Kyoto Collection of human embryos and fetuses: History and recent advancements in modern methods. Cells Tissues Organs. 2018; 205:314–319. https://doi.org/10.1159/000490672 PMID: 30064127
13. Shiota K, Yamada S, Nakatsu-Komatsu T, Uwabe C, Kose K, Matsuda Y, et al. Visualization of human prenatal development by magnetic resonance imaging (MRI). Am J Med Genet A. 2007; 143A:3121–3126. https://doi.org/10.1002/ajmg.a.31994 PMID: 17963260
14. Matsuda Y, Utsuzawa S, Kurimoto T, Haishi T, Yamazaki Y, Kose K, et al. Super-parallel MR microscope. Magn Reson Med. 2003; 50:183–189. https://doi.org/10.1002/mrm.10515 PMID: 12815693

15. Kumano Y, Tanaka S, Sakamoto R, Kanahashi T, Imai H, Yoneyama A, et al. Upper arm posture during human embryonic and fetal development. Anat Rec (Hoboken). 2022; 305:1682–1691. https://doi.org/10.1002/ar.24796 PMID: 34605199

16. Moore KL, Persaud TVN, Torchia MG. The limbs. In: Moore KL, Persaud TVN, Torchia MG, editors. The developing human: clinically oriented embryology. 8th ed. Saunders/Elsevier; 2008. pp. 365–379.

17. Moore KL, Persaud TVN, Shiota K. The third to eighth weeks of human development. In: Moore KL, Persaud TVN, Shiota K, editors. Color atlas of clinical embryology. 1st ed. Philadelphia: Saunders; 1994. pp. 9–61.

18. Tuchmann-Duplessis H, Haegel P. Illustrated human embryology. Organogenesis. New York: Springer-Verlag; 1972.

19. FitzGerald MJT, FitzGerald M. Human embryology. Bailliere Tindall; 1995.

20. Tanaka S, Sakamoto R, Kanahashi T, Yamada S, Imai H, Yoneyama A, et al. Shoulder girdle formation and positioning during embryonic and early fetal human development. PLoS One. 2020; 15:e0238225. https://doi.org/10.1371/journal.pone.0238225 PMID: 32915841

21. Gardner E, Gray DJ. Prenatal development of the human hip joint. Am J Anat. 1950; 87:163–211. https://doi.org/10.1002/aja.1000870202 PMID: 14771010

22. Uhthoff HK. The development of the hip. In: Uhthoff HK, editor. The embryology of the human locomotor system. Berlin: Springer-Verlag; 1990. pp. 117–127.

23. de Bakker BS, de Jong KH, Hagoort J, de Bree K, Besselink CT, de Kanter FE, et al. An interactive three-dimensional digital atlas and quantitative database of human development. Science. 2016; 354:6315. https://doi.org/10.1126/science.aag0053 PMID: 27884980

24. Dawood Y, Buijtendijk MFJ, Shah H, Smit JA, Jacobs K, Hagoort J, et al. Imaging fetal anatomy. Semin Cell Dev Biol. 2022; 131: 78–9. https://doi.org/10.1016/j.semcdb.2022.02.023 PMID: 35282997